ORIGINAL ARTICLE

Nano-clay assisted pore refinement and performance enhancement in rubberized alkali-activated composites

Ahmet Benli · Bayram Sönmez · Ali Öz · Adem Yar · Oğuzhan Yavuz Bayraktar · Gökhan Kaplan

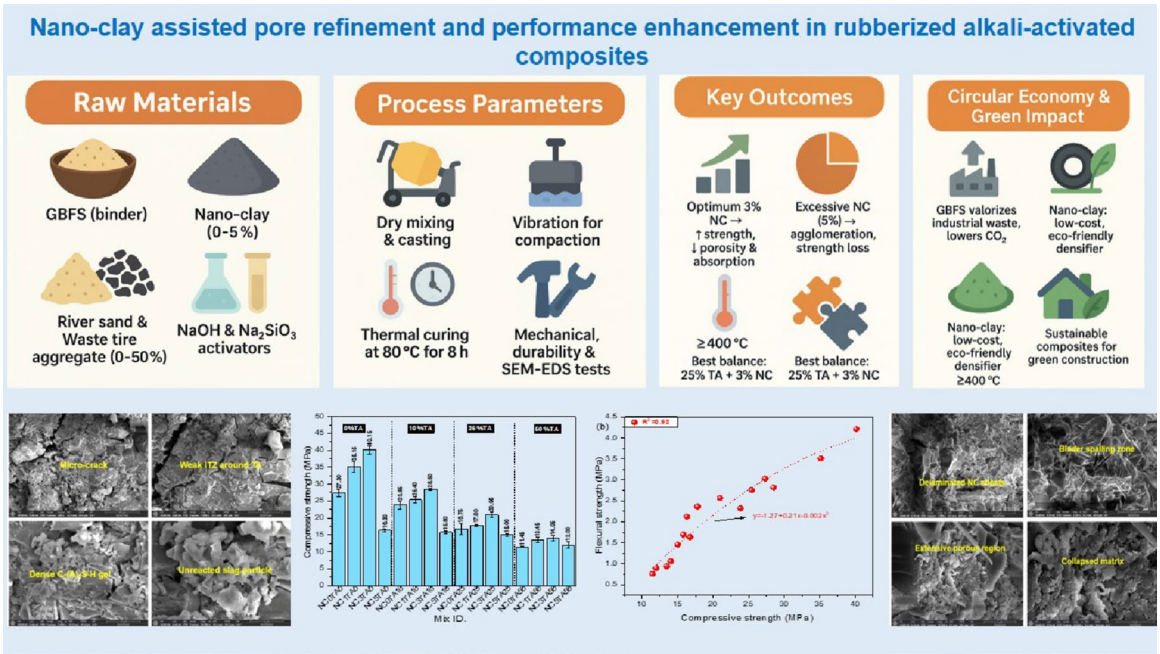
Received: 19 November 2025 / Revised: 20 July 2026 / Accepted: 30 July 2026
© Wroclaw University of Science and Technology 2026

Abstract

This study investigates the synergistic effects of nano-clay (NC) incorporation and waste tire aggregate (TA) substitution on the mechanical, thermal, and durability performance of alkali-activated composites (AACs). Ground granulated blast furnace slag (GBFS) served as the primary precursor, with NC introduced at 0–5% by binder weight and TA replacing river sand at 0–50% by volume. Specimens were thermally cured at 80 °C for 8 h and evaluated for compressive and flexural strength, oven-dry density, porosity, water absorption, sorptivity, thermal resistance, freeze–thaw durability, and sulfate attack resistance, supported by SEM–EDS microstructural analysis. Results showed that moderate NC addition (≈3%) significantly enhanced matrix densification, yielding peak compressive (40.15 MPa) and flexural strengths (4.21 MPa) with reduced porosity (6.79%), water absorption (5.35%), and sorptivity (1.27). In contrast, excessive NC (5%) caused agglomeration, increased porosity, and strength loss. TA replacement consistently reduced strength and density due to weak interfacial bonding and high porosity, though moderate dosages (≤25%) partially balanced sustainability with performance. Under sulfate attack, the 25%TA–3%NC mixture exhibited the lowest strength loss (5.87%), while thermal tests revealed that NC improved resistance up to 200 °C, whereas TA mitigated degradation at ≥400 °C by providing stress-relief through its elastic nature. Freeze–thaw tests confirmed superior durability for NC-densified matrices compared to TA-rich systems. the findings highlight that optimizing NC content (~3%) and maintaining moderate TA levels (≤25%) yields eco-efficient AACs with balanced mechanical, durability, and thermal properties, offering a sustainable valorization route for industrial and end-of-life waste materials.

Published online: 11 August 2026

Graphical abstract



Keywords Alkali-activated composites · Nano clay · Waste tire aggregate · Thermal resistance · Sulfate durability · Freeze–thaw performance

1 Introduction

The global construction sector faces a dual challenge: meeting the demand for durable infrastructure while reducing environmental burdens [1]. Ordinary Portland cement (OPC), still the primary binder in concrete [2], contributes 7–8% of global CO_2 emissions [3] due to limestone calcination and fuel use in clinker production [4]. Cement manufacture also consumes vast raw materials and energy [5], intensifying concerns over climate change and resource depletion [6]. These challenges have motivated research into eco-efficient alternatives [7] that provide comparable or superior performance [8] with lower environmental impact [9].

Alkali-activated materials (AAMs) [10]and geopolymers have emerged as promising candidates [11], as they valorize industrial by-products [12], exhibit excellent mechanical and durability properties [13], and significantly reduce embodied carbon [14]. Alkali-activated composites (AACs) are synthesized by activating aluminosilicate-rich precursors [15] with alkaline solutions such as sodium hydroxide (NaOH) and sodium silicate (Na_2SiO_3) [16]. Unlike OPC hydration, which mainly produces calcium silicate hydrate (C-S-H), alkali activation yields calcium-aluminosilicate-hydrate (C-(A)-S-H), sodium-aluminosilicate-hydrate (N-A-S-H) [17], and hybrid gels that impart superior chemical resistance, thermal stability, and strength [18]. Ground granulated blast furnace slag (GBFS) is especially attractive due to its high amorphous content [19], calcium oxide, and reactive silica-alumina composition, enabling rapid gel formation [20]. Nevertheless, challenges such as shrinkage [21], porosity, and brittleness persist [22], requiring complementary additives [23] and waste-derived materials to optimize AAC performance [24].

One strategy that has gained increasing attention is the incorporation of nanomaterials [25] into alkali-activated systems [26]. Nanoparticles, owing to their extremely high surface area and reactivity [27], can serve as nucleation sites, accelerate geopolymerization [28], refine pore structures, and enhance the interfacial transition zone (ITZ) [29]. Among various nanomaterials, nano-clay (NC) has been identified as a cost-effective, widely

available, and environmentally benign additive [30]. NC, particularly montmorillonite- or smectite-type particles, exhibits a layered silicate structure, high cation exchange capacity, and significant surface reactivity [31], making it highly effective in modifying cementitious and alkali-activated binders [32]. Previous studies have demonstrated that the inclusion of NC at low dosages (typically 1–3% by binder weight) enhances compressive and flexural strengths, reduces permeability, and improves durability against chloride ingress, sulfate attack, and carbonation. This improvement is attributed to the ability of NC lamellae to fill micro voids, densify the binder matrix, and promote additional gel formation. However, excessive NC addition often leads to agglomeration, poor dispersion, increased viscosity of the fresh mixture, and consequently reduced workability and mechanical performance. Thus, optimizing the dosage of NC is essential for achieving maximum benefits. Assaedi et al. [33] investigated the effect of 0–3% NC on the thermal and hardened properties of fly ash (FA)-based geopolymers. SEM analysis revealed the presence of unreacted and partially reacted FA particles, while the addition of 1–3% NC increased density and reduced the proportion of unreactive phases [30]. Shahrajabian and Behfarnia [34] showed that compressive strength decreased with more freeze–thaw cycles, but mixes with 2% NC had the least loss. NC-modified concretes retained higher strength than the control, though density declined due to freeze-thaw damage. Mass loss was mainly linked to edge deterioration. Similarly, Gadkar and Subramaniam [35] found that 2% NC improved microstructure, reduced porosity and water absorption, and enhanced freeze-thaw resistance, thus improving durability.

Parallel to binder modification, aggregate substitution with recycled or waste-derived materials represents another crucial pathway for enhancing the sustainability of AACs [36]. Among various waste streams, end-of-life tires pose one of the most pressing environmental challenges worldwide, with millions of tons discarded annually and often ending up in landfills or illegal dumps [37]. Tire waste is highly durable, non-biodegradable, and resistant to natural degradation [38], thereby posing long-term environmental and health hazards [39]. Recycling waste tires into value-added construction materials offers a dual benefit [40]: it reduces the burden on landfills, mitigates the extraction of natural aggregates [41], and supports sustainable waste management strategies aligned with circular economy principles [42]. Similar approaches have also been successfully applied to other industrial waste streams, where the incorporation of binder systems enhances waste stabilization, improves environmental performance, and promotes long-term sustainable utilization [43].Waste tire aggregates (TA), typically produced by shredding and grinding end-of-life tires into granulated rubber particles, can be employed as partial replacements for natural sand in concrete and AACs [44]. The inclusion of TA reduces the density of composites, improves thermal and acoustic insulation, and contributes to circular economy objectives by valorizing an otherwise problematic waste [45]. Nevertheless, TA incorporation also introduces significant challenges: its hydrophobic surface chemistry, low stiffness, and porous structure result in weak bonding with the binder matrix, reduced load-bearing capacity, and increased porosity [46]. As a result, the mechanical performance of rubberized concretes and AACs often deteriorates [42], especially at high replacement levels, although moderate dosages ($\leq 25\%$) may achieve acceptable trade-offs between sustainability and structural requirements [47].

The simultaneous use of NC and waste tire aggregate in alkali-activated composites offers an intriguing research direction. NC can potentially counteract some of the detrimental effects associated with TA incorporation by refining the pore structure, enhancing matrix densification, and strengthening the ITZ. For instance, while TA tends to increase porosity and reduce strength, NC can mitigate these issues by promoting additional gel formation and improving compactness. Moreover, the lamellar structure of NC may interact with the rough, porous surfaces of rubber particles, enhancing interfacial bonding and reducing micro cracking. Such synergistic effects have been hypothesized but remain insufficiently explored in the existing literature, particularly within GBFS-based AAC systems [48]. Although separate studies have examined the benefits of NC addition and the challenges of TA incorporation, comprehensive investigations into their combined influence on mechanical properties, thermal resistance, and long-term durability are still scarce. This knowledge gap underscores the need for systematic research that simultaneously addresses binder densification and sustainable aggregate substitution.

Durability is another critical consideration in the development of eco-efficient AACs. In real-world service conditions, construction materials are often subjected to aggressive environments such as sulfate-rich soils,

freeze–thaw cycles in cold climates, and elevated temperatures due to fire exposure or thermal processes [49]. In addition, recent studies on hydraulic structures have shown that abrasion induced by water-particle interaction leads to surface degradation and microstructural damage, highlighting the critical role of pore structure and interfacial integrity in durability performance. Similarly, recent reviews on waste-based geopolymer systems confirm that optimized incorporation of industrial by-products enhances pore refinement and durability, while excessive content increases porosity and micro cracking [50]. Sulfate attack, particularly from magnesium sulfate ($MgSO_4$), is known to cause decalcification of binding gels, formation of expansive secondary phases (e.g., gypsum and brucite), and eventual cracking and strength loss. Freeze-thaw cycles induce repeated expansion and contraction within pore water, leading to micro cracking, scaling, and deterioration of mechanical integrity [51]. Elevated temperatures, meanwhile, can cause dehydration of binding gels, shrinkage, and collapse of the microstructure, especially above 400–600 °C. Conventional OPC-based concretes are highly vulnerable to such degradation processes, whereas AACs generally exhibit improved chemical resistance and thermal stability [52]. Nevertheless, their long-term durability is highly dependent on mix design parameters, curing regimes, and the type and proportion of additives used. Therefore, assessing the combined influence of NC and TA on the sulfate, freeze–thaw, and thermal resistance of AACs is essential for determining their suitability in demanding service environments.

Several researchers have already highlighted the potential of hybrid approaches in tailoring AAC performance. For instance, the inclusion of nano-silica, nano-alumina [53], or NC has been shown to improve sulfate resistance by reducing pore connectivity and hindering ion ingress [54]. Similarly, lightweight aggregates such as expanded perlite, pumice, or rubber particles have been investigated for their role in improving thermal shock resistance [55], albeit often at the expense of mechanical strength [56]. However, the combined role of nanomaterial-assisted pore refinement and rubber-induced strain accommodation has not been systematically examined. Understanding this interaction could provide a unique pathway for designing AACs that balance mechanical strength with thermal and chemical durability. Additionally, from a sustainability perspective, the dual valorization of industrial by-products (GBFS) and end-of-life waste (rubber tires) aligns with circular economy principles and global targets for carbon reduction and waste minimization.

Given this background, the present study comprehensively investigates the synergistic role of NC and waste tire aggregate (TA) in GBFS-based AACs. The research objectives are fourfold: (i) to examine the effects of NC dosage (0–5%) and TA substitution (0–50%) on mechanical properties such as compressive and flexural strength; (ii) to assess their influence on physical characteristics including density, porosity, water absorption, and sorptivity; (iii) to evaluate durability under sulfate exposure, freeze–thaw cycles, and elevated temperatures; and (iv) to elucidate the underlying mechanisms through scanning electron microscopy (SEM) and energy-dispersive spectroscopy (EDS) analyses. By addressing these aspects, the study identifies optimal mix proportions that balance sustainability with structural and durability requirements.

The novelty of this study lies not simply in the combined use of NC and TA, but in the systematic and mechanism-oriented evaluation of their coupled effects within GBFS-based alkali-activated composites. Unlike previous studies that have primarily investigated nano-modification or recycled aggregate incorporation independently, this work examines the interaction between nano-scale pore refinement induced by NC and macro-scale mechanical behavior governed by deformable TA particles. In this context, the study establishes a unified performance-microstructure relationship by integrating mechanical, physical, and durability properties-including sulfate resistance, freeze-thaw performance, and high-temperature behavior-with SEM-EDS observations. The results reveal a coupled and partially competing mechanism, where NC enhances matrix densification and gel formation, while TA introduces interfacial weaknesses but simultaneously contributes to stress redistribution and thermal strain accommodation.

Table 1 Chemical properties of GBFS and NC (% wt)

	CaO	SiO_2	Al_2O_3	Fe_2O_3	MgO	Na_2O	K_2O	SO_3	LOI
GBFS	38.3	32.6	9.6	2.1	14.6	0.6	0.9	0.5	0.7
NC	0.3	56.4	19.8	4.8	1.3	0.6	1.3	0.1	15.3

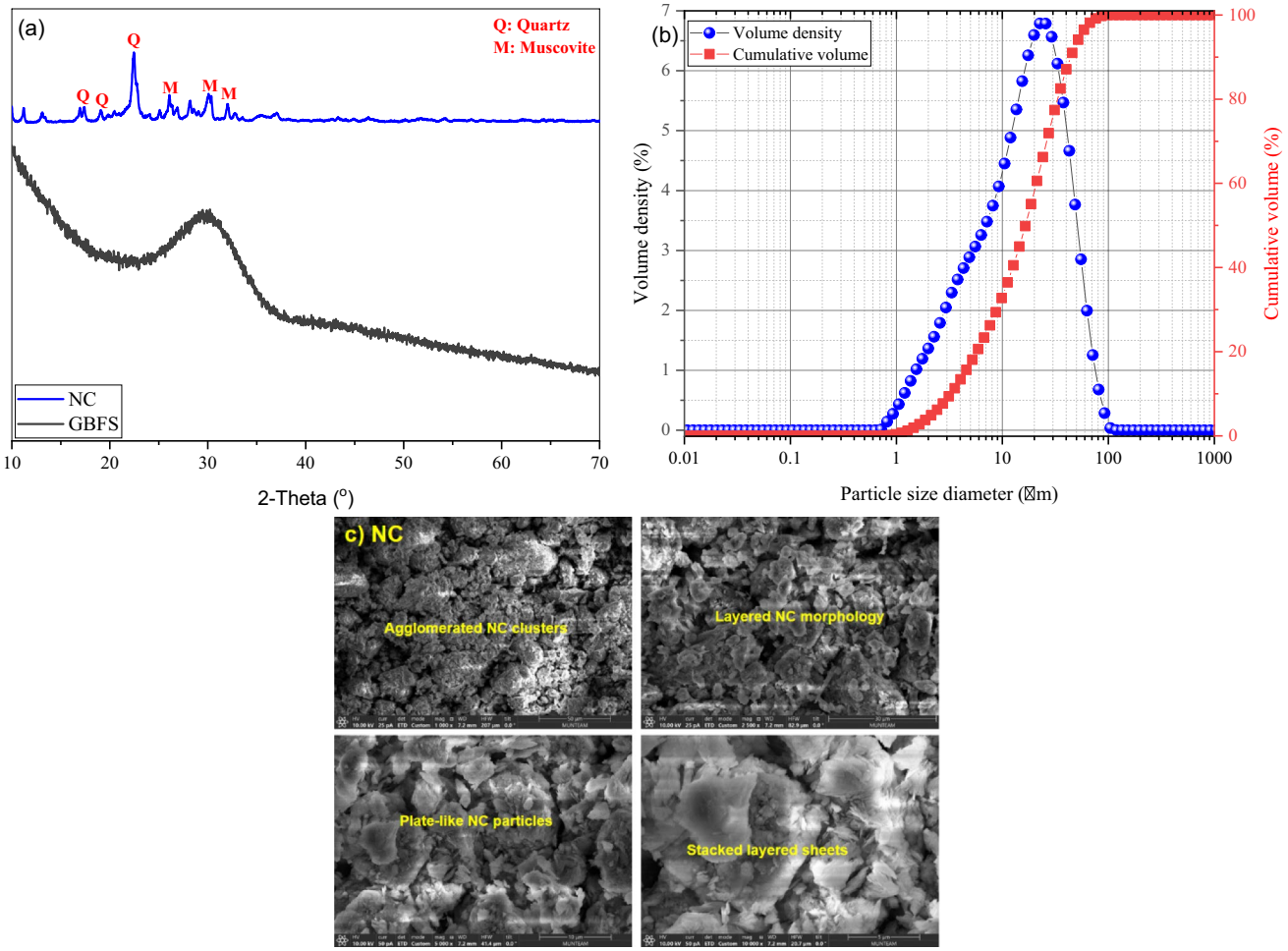


Fig. 1 **a** XRD pattern of GBFS and NC **b** size distribution of GBFS **c** SEM images of NC

2 Materials and methods

2.1 Materials

Ground granulated blast furnace slag (GBFS) was selected as the primary aluminosilicate precursor due to its high CaO (38.3%) and SiO_2 (32.6%) contents, which favor the formation of calcium-rich hydration products and geopolymeric gels under alkaline conditions, while its notable MgO content (14.6%) can further contribute to secondary phases such as hydrotalcite-like structures. The chemical compositions of GBFS and nano-clay (NC) determined by XRF analysis are presented in Table 1. NC was rich in SiO_2 (56.4%) and Al_2O_3 (19.8%), with appreciable Fe_2O_3 (4.8%) and a relatively high loss on ignition (15.3%), reflecting the presence of structural water and volatile matter within its layered aluminosilicate framework. The mineralogical and morphological characteristics of these precursors are shown in Fig. 1: GBFS exhibited a broad amorphous hump at 25°–35° 2θ in its XRD pattern (Fig. 1a), confirming its predominantly vitreous nature with only minor crystalline peaks

 https://doi.org/10.1007/s43452-026-01614-2

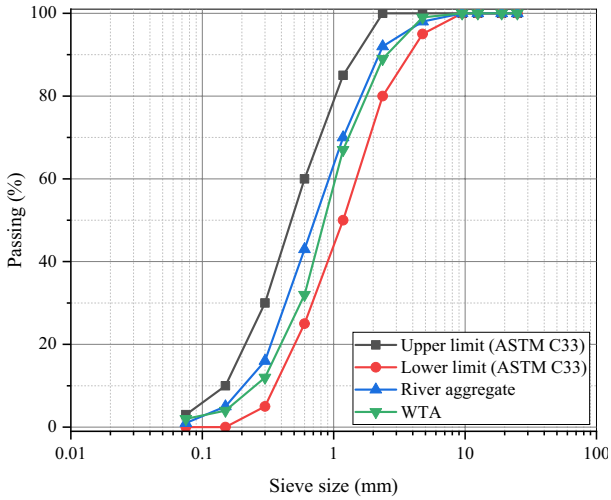


Fig. 2 Particle size distribution of river sand and waste tire aggregate

Table 2 Properties of sands

	Specific gravity	Water absorption (24 h)	Sieve size	Fineness modulus
River sand	2.58	2.34%	0–4 mm	2.73
Tire aggregate	1.09	1.90%	0–4 mm	2.41

of gehlenite, akermanite, and quartz, which explains its high reactivity under alkaline activation. In contrast, NC displayed sharp basal reflections around $2\theta \approx 7°$, 20°, and 27°, indicative of smectite/montmorillonite-type structures with interlayer water and cations that promote surface reactivity and ion exchange, thus enhancing nucleation and gel stability in alkali-activated matrices. SEM micrographs of NC (Fig. 1c) revealed thin, plate-like lamellae (tens of nanometers thick, extending laterally to several hundred nanometers) with rough edges and stacked aggregates, providing high surface area and abundant active sites that can accelerate geopolymerization by serving as nucleation centers for C–(A)–S–H and N–A–S–H gels. While this morphology improves pore refinement and densification by obstructing capillary pathways, excessive NC (> 3%) tends to agglomerate due to van der Waals forces, generating clusters and voids that impair homogeneity and mechanical strength. GBFS particles (Fig. 1b) were angular and irregular in shape, consistent with their ground vitreous origin, which increases packing density and dissolution rate, thereby facilitating strength development.

For fine aggregates, natural river sand (RS) and waste tire aggregate (TA) were used, with their grading curves shown in Fig. 2 and physical properties summarized in Table 2. RS had higher specific gravity (2.58) and fineness modulus (2.73), ensuring compactness and stability, whereas TA exhibited a much lower density (1.09) and fineness modulus (2.41), reflecting its lightweight and porous structure. TA also had slightly lower water absorption (1.90%) than RS (2.34%) because of its hydrophobic rubber surface, though its irregular pores introduce weak interfacial transition zones (ITZs) that can reduce mechanical performance. The contrasting properties of RS and TA thus allowed the design of composites balancing density reduction, sustainability, and durability. Finally, sodium hydroxide (NaOH, 12 M) and sodium silicate (Na_2SiO_3; $SiO_2/Na_2O \approx 2.1$, solids content ≈ 40%) were employed as alkaline activators, prepared at least 24 h before mixing to ensure complete dissolution and stabilization; NaOH provided the high alkalinity necessary for aluminosilicate dissolution, while Na_2SiO_3 supplied reactive silicate species to promote polycondensation and cross-linked gel formation. Collectively, the amorphous, Ca-rich GBFS, the layered and highly reactive NC, the dense RS, the lightweight TA, and the synergistic alkaline activators together formed a versatile material system aimed at producing alkali-activated composites with enhanced microstructural integrity, mechanical strength, and environmental sustainability.

2.2 Mix design strategy and processing of alkali-activated composites

The alkali-activated composite (AAC) mixtures were designed according to a factorial approach that considered two main variables: the incorporation of nano-clay (NC) as a partial replacement of ground granulated blast furnace slag (GBFS), and the substitution of natural river sand (RS) with waste tire aggregate (TA). This strategy aimed to systematically evaluate the microstructural, mechanical, and durability responses of AACs to varying binder modification and aggregate replacement levels, thereby identifying optimum combinations for eco-efficient, high-performance composites. The detailed mixture compositions and constituent quantities are presented in Table 3.

In the binder system, GBFS was consistently used as the primary precursor at a baseline dosage of 800 kg/m³, while NC was introduced at 0%, 1%, 3%, and 5% by weight of the binder. This stepwise inclusion enabled a clear assessment of the beneficial effects of NC-such as enhanced nucleation, pore refinement, and gel densification-against the detrimental risks associated with excessive dosage, including agglomeration, increased viscosity, and poor dispersion. On the aggregate side, RS was the reference material, while TA was incorporated at 0%, 10%, 25%, and 50% by volume, replacing an equivalent portion of RS. This allowed investigation of how lightweight, porous, and hydrophobic rubber particles influenced the density, porosity, and interfacial transition zone (ITZ) characteristics of the composites. At 10% replacement, TA was expected to provide modest density reduction with limited strength loss, while higher levels (25–50%) were anticipated to significantly compromise compactness and bonding, despite offering sustainability benefits by valorizing recycled tire waste.

The alkaline activator solution consisted of 12 M sodium hydroxide (NaOH) and sodium silicate (Na_2SiO_3, $SiO_2/Na_2O \approx 2.1$, solids ≈ 40%), applied at a constant dosage across all mixtures. The fixed activator-to-binder ratio ensured that observed variations in performance could be attributed to NC and TA rather than changes in alkalinity or silicate availability. The activator dosage and A/B ratio were intentionally kept constant across all mixtures to ensure a controlled experimental framework. This approach enables the direct assessment of the individual and coupled effects of NC and TA without introducing additional variability related to changes in activator content. NaOH provided sufficient alkalinity for the dissolution of the amorphous GBFS matrix, while Na_2SiO_3 supplied soluble silicates to promote cross-linked gel formation (C-(A)-S-H and N-A-S-H phases), thus reinforcing the matrix structure. No additional mixing water, plasticizer, or superplasticizer was incorporated into any mixture. The liquid content and activator-to-binder ratio were maintained constant throughout the experimental program to ensure that the effects of nano-clay dosage and waste tire aggregate replacement could be evaluated

Table 3 Mixture compositions and material contents (kg/m³)

Mix ID	NC (%)	TA (%)	GBFS	NC	NH	NS	RS	TA
NC0TA0	0	0	800.0	0.0	196.8	491.2	528.4	0.0
NC1TA0	1		792.0	8.0	196.8	491.2	527.2	0.0
NC3TA0	3		776.0	24.0	196.8	491.2	524.7	0.0
NC5TA0	5		760.0	40.0	196.8	491.2	522.3	0.0
NC0TA10	0	10	800.0	0.0	196.8	491.2	475.5	21.6
NC1TA10	1		792.0	8.0	196.8	491.2	474.4	21.5
NC3TA10	3		776.0	24.0	196.8	491.2	472.3	21.4
NC5TA10	5		760.0	40.0	196.8	491.2	470.1	21.3
NC0TA25	0	25	800.0	0.0	196.8	491.2	396.3	53.9
NC1TA25	1		792.0	8.0	196.8	491.2	395.4	53.8
NC3TA25	3		776.0	24.0	196.8	491.2	393.5	53.6
NC5TA25	5		760.0	40.0	196.8	491.2	391.7	53.3
NC0TA50	0	50	800.0	0.0	196.8	491.2	264.2	107.8
NC1TA50	1		792.0	8.0	196.8	491.2	263.6	107.6
NC3TA50	3		776.0	24.0	196.8	491.2	262.4	107.1
NC5TA50	5		760.0	40.0	196.8	491.2	261.2	106.7

without the influence of workability-modifying admixtures. Consequently, the reduced workability observed at higher NC contents (particularly 5%) was considered an inherent characteristic of the mixture and was intentionally not compensated by adjusting the water or admixture content.

For specimen preparation, dry constituents (GBFS, NC, RS, and TA) were first thoroughly homogenized to prevent nano-clay agglomeration and to achieve uniform dispersion within the slag matrix. The pre-prepared alkaline solution, which had been left to stabilize for 24 h, was then gradually added to the dry mix under mechanical stirring until a workable paste was achieved. Fresh mixtures were cast into steel molds of $40 \times 40 \times 160$ mm prisms for flexural and compressive strength testing, as well as 50 mm cubes for physical and durability evaluations. To ensure proper consolidation, specimens were vibrated to eliminate entrapped air bubbles, thereby minimizing initial porosity. Immediately after casting, molds were sealed to avoid premature moisture evaporation and transferred to a curing chamber at 80 °C for 8 h. This thermal curing regime was selected to accelerate the geopolymerization process, promote early strength development, and stabilize the microstructure by enhancing gel crystallization and binder densification. Following curing, specimens were demolded and stored under laboratory conditions until testing.

This mix design approach allowed for a systematic exploration of the balance between microstructural densification induced by NC and the sustainability gains from TA incorporation. It provided a robust framework to determine how low NC dosages ($\approx$3%) and moderate TA levels ($\leq$25%) could synergistically improve performance, while also identifying the thresholds beyond which excessive NC or TA additions become detrimental. This methodological strategy ensured that the experimental program could not only capture strength and durability trends, but also provide insights into the underlying mechanisms governing the observed behaviors.

2.3 Test methods

To comprehensively evaluate the performance of the alkali-activated composites (AACs), a series of standardized tests were conducted focusing on mechanical, physical, durability, and microstructural properties. The specific procedures and standards followed are outlined below.

2.3.1 Mechanical properties

Flexural strength tests were performed in accordance with ASTM C348 [57] using prism specimens of dimensions 40 × 40 × 160 mm. This method assesses the material's resistance to bending-induced cracking and is essential for evaluating structural performance under tensile stress. Compressive strength was determined based on ASTM C349 [58], which involves testing the halves of prisms previously used in flexural strength evaluation. These tests were conducted after thermal curing at 80 °C, enabling the assessment of strength development under elevated curing conditions.

2.3.2 Physical properties

Apparent porosity, water absorption, and oven-dry density were measured following ASTM C642 [59] using cube specimens of 50 × 50 × 50 mm. These properties provide insights into pore connectivity, matrix compactness, and the material's resistance to moisture ingress. All physical tests were performed after thermal curing at 80 °C to capture stabilized material behavior.

2.3.3 Thermal resistance

Thermal stability was assessed by exposing 50 mm cube specimens to elevated temperatures of 200 °C, 400 °C, and 600 °C. Samples were placed in a muffle furnace and heated at a rate of 5 °C/min until the target temperature

was reached [60], followed by a 2-hour dwell time [61]. After natural cooling, specimens were tested for weight loss and residual compressive strength to determine the impact of thermal exposure on mechanical integrity.

2.3.4 Sorptivity

Capillary water absorption was measured using the TS EN 1015-18 [62] standard, which evaluates water sorptivity by monitoring the mass gain of thermally cured specimens over time. This parameter is critical for assessing moisture transport properties and predicting long-term durability in humid or aggressive environments.

2.3.5 Sulfate resistance

To simulate sulfate-rich environments, specimens cured at 80 °C were immersed in a 5% $MgSO_4$ solution for 120 days. Changes in mass and compressive strength were recorded post-exposure to determine the resistance of AACs to chemical degradation, particularly from sulfate-induced decalcification and formation of expansive phases.

2.3.6 Freeze–thaw resistance

Freeze–thaw durability was evaluated according to ASTM C666 [63], which subjects concrete specimens to 120 cycles of rapid freezing and thawing. This test investigates the material's ability to resist mechanical and surface deterioration under cyclic thermal stresses, simulating cold-climate applications.

2.3.7 Microstructural analysis

Scanning electron microscopy (SEM) coupled with energy-dispersive X-ray spectroscopy (EDS) was employed to investigate the microstructure of selected specimens. Analyses were conducted after thermal curing at 80 °C, after exposure to 600 °C, and following 120 days of sulfate immersion. The observations focused on gel morphology, pore structure, cracking features, and fiber–matrix interactions, with elemental mapping used to identify sulfate-related degradation products. These microstructural insights were correlated with mechanical and durability test results to better explain performance at the micro scale.

2.3.8 Experimental workflow

A schematic overview of the entire experimental procedure-from raw material preparation through mixing, casting, curing, and subsequent testing-is presented in Fig. 3. The diagram illustrates each stage of the study in a step-by-step manner, beginning with the selection and characterization of raw materials, followed by the batching and homogenization of mixtures, specimen casting, and the application of thermal curing regimes. It then outlines the sequence of mechanical, physical, durability, and microstructural analyses conducted to evaluate performance. By providing this visual summary, the methodology is conveyed in a clear and systematic format, thereby enhancing transparency and ensuring reproducibility of the research.

3 Results and discussion

3.1 Compressive strength

Figure 4 presents the influence of incorporating nano-clay (NC) at different replacement levels of ground granulated blast furnace slag (0, 1, 3, and 5%) and substituting river sand (RS) with waste tire aggregate (TA) (0, 10, 25,

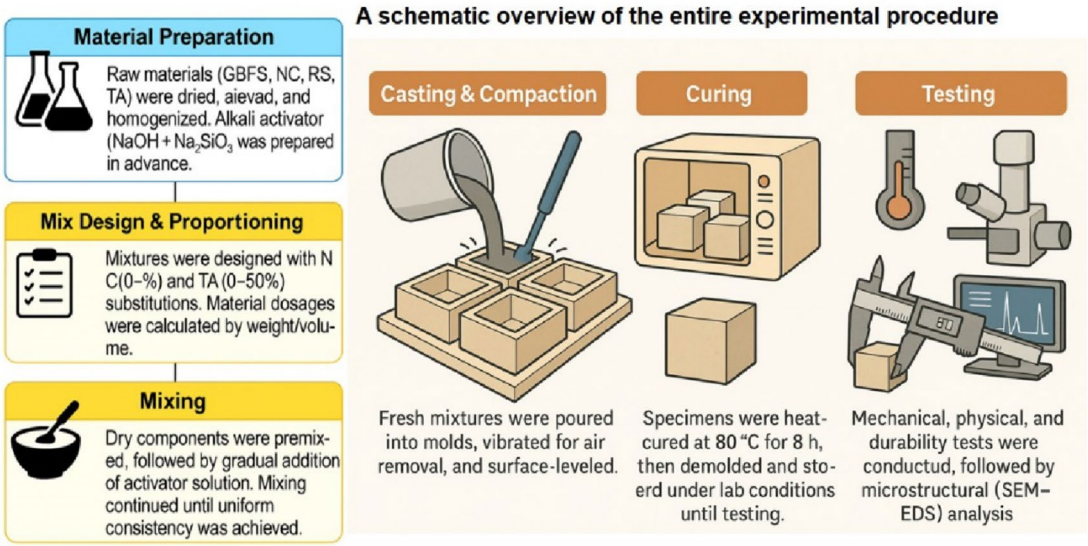
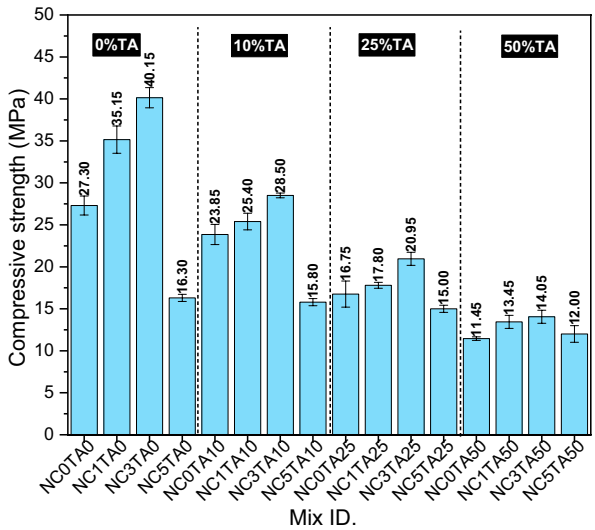


Fig. 3 Experimental framework for the fabrication and evaluation of AACs

Fig. 4 Compressive strength results



and 50%) on the compressive strength of alkali-activated composites (AACs) thermally cured at 80 °C for 8 h. The results reveal clear trends in both the beneficial and detrimental effects of NC dosage and TA incorporation.

For the reference mixtures containing 100% RS, the compressive strength increased from 27.3 MPa at 0%NC to 35.15 MPa at 1%NC and peaked at 40.15 MPa at 3%NC, reflecting an overall improvement of about 47% compared to the unmodified mixture [64]. This enhancement can be attributed to the high surface area and surface reactivity of NC, which provided abundant nucleation sites, accelerated geopolymerization reactions [65], and promoted the formation of additional binding gels (C–(A)–S–H and N–A–S–H) [66], thereby contributing to matrix densification [67]. However, at 5%NC, the compressive strength drastically decreased to 16.30 MPa, representing a 59% reduction compared to the optimum (3%NC). This decline is associated with the excessive fineness and high water demand of NC, which can lead to particle agglomeration, poor dispersion [68], increased viscosity of the fresh mixture, and reduced workability [69]. Consequently, an optimum dosage of NC is essential, beyond which its role shifts from being beneficial to detrimental.

The mixtures with partial RS replacement by TA exhibited similar patterns but with generally lower strength values. In the 90%RS + 10%TA series, compressive strength rose modestly from 23.85 MPa at 0%NC to 25.40 MPa at 1%NC and reached 28.50 MPa at 3%NC, a gain of about 19.5%. However, further addition to 5%NC reduced the strength to 15.80 MPa, indicating a ~ 45% decrease relative to the optimum. This trend demonstrates that although NC could mitigate the strength loss caused by limited TA incorporation, it could not entirely restore the performance to the level of 100%RS mixtures.

With higher TA content, the beneficial impact of NC became increasingly constrained. For the 75%RS + 25%TA mixture, strength improved from 16.75 MPa at 0%NC to 20.95 MPa at 3%NC (≈ 25% increase), but decreased again to 15.0 MPa at 5%NC, below the original reference value. The 50%RS + 50%TA series yielded the lowest strengths, increasing only from 11.45 MPa at 0%NC to 14.05 MPa at 3%NC (≈ 22.7% increase), then falling to 12.0 MPa at 5%NC. In these mixes, the weak bonding and high deformability of rubber particles dominated the mechanical response, limiting the positive effect of NC.

When the mixtures are compared at the optimal 3%NC level, the detrimental effect of TA substitution becomes clear. The compressive strength declined progressively with increasing TA: 40.15 MPa for 0%TA, 28.50 MPa for 10%TA (≈ 29% reduction), 20.95 MPa for 25%TA (≈ 48% reduction), and 14.05 MPa for 50%TA (≈ 65% reduction). This reduction is attributed to the porous and hydrophobic nature of rubber aggregates, which create weak interfacial transition zones (ITZs) [36], induce stress concentrations under load, and increase overall porosity of the composite. The elastic behavior of TA further reduces the load-bearing capacity of the matrix, leading to lower compressive strength [70].

The results confirm two important findings. First, the incorporation of a small amount of NC (around 3%) is highly effective in promoting matrix densification, improving geopolymer gel formation, and enhancing compressive strength, provided the mixture contains limited or no TA. Second, although NC offers partial improvements at moderate levels of TA replacement, it cannot fully counteract the negative effects of rubber aggregate inclusion at higher dosages. Excessive NC content (5%) or high TA ratios both act detrimentally, resulting in significant strength loss. The best-performing mixture was obtained with 100%RS and 3%NC, which achieved a compressive strength of 40.15 MPa, while the poorest performance was observed in mixtures with either 100%RS + 5%NC (16.30 MPa) or 50%RS + 50%TA + 5%NC (12.0 MPa).

3.2 Flexural strength

Figure 5a shows the influence of incorporating NC as a partial replacement for GBFS at levels of 0, 1, 3, and 5%, combined with RS substitution by TA at 0, 10, 25, and 50%, on the flexural strength of AACs cured at 80 °C for 8 h. The results reveal that both NC content and TA replacement strongly affected the bending performance of the composites, with clear improvement at moderate NC levels and sharp deterioration at excessive NC dosages or high TA contents.

For the control series containing 100% RS, the flexural strength increased progressively from 3.03 MPa at 0%NC to 3.52 MPa at 1%NC, before peaking at 4.21 MPa at 3%NC. This represents a gain of approximately 39% compared with the unmodified mixture. Such improvement can be attributed to the high surface area and reactivity of NC, which enhances geopolymerization kinetics, promotes gel phase formation, and provides better particle packing. However, a further increase to 5%NC drastically reduced the flexural strength to 2.12 MPa, corresponding to a 50% loss relative to the optimum. This sharp decline indicates that excessive NC addition leads to poor dispersion, agglomeration, and increased water demand, resulting in reduced workability and the formation of weak zones that accelerate crack initiation and propagation under flexural loading.

A similar but less pronounced trend was observed when 10% of RS was replaced with TA. The flexural strength increased from 2.32 MPa at 0%NC to 2.76 MPa at 1%NC, then slightly to 2.82 MPa at 3%NC, reflecting a modest gain of about 21.6%. However, at 5%NC the strength fell sharply to 1.70 MPa, approximately 40% lower than at 3%NC. These results demonstrate that small additions of NC were able to partially compensate for the

 https://doi.org/10.1007/s43452-026-01614-2

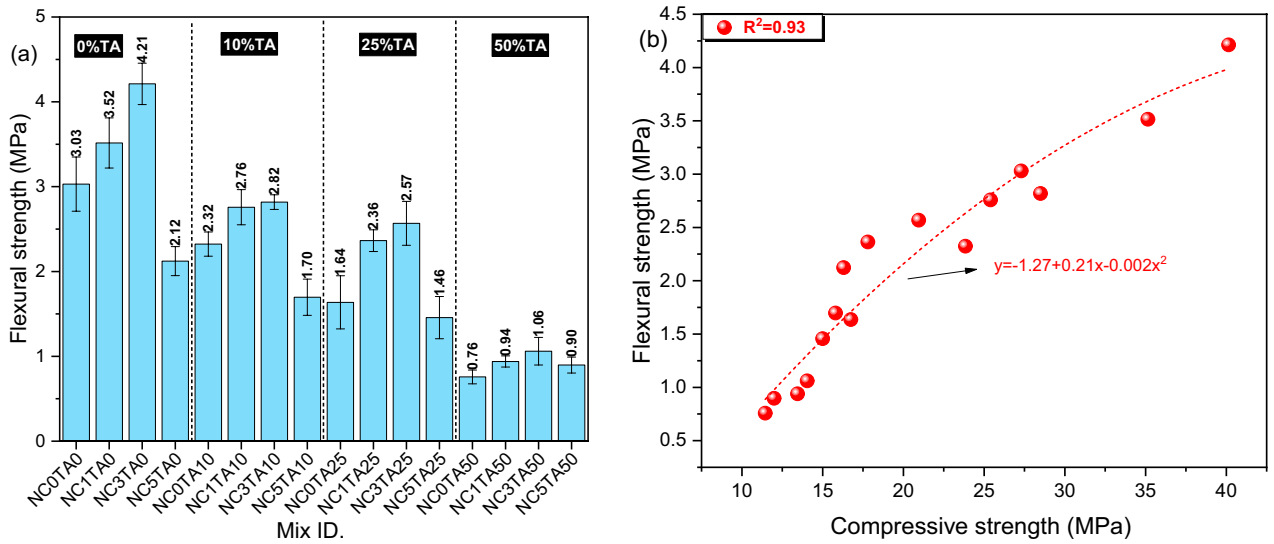


Fig. 5 **a** Flexural strength results **b** compressive strength vs. flexural strength

detrimental effect of rubber aggregates by strengthening the binder matrix, but the inherent weaknesses of TA, including its porous structure, hydrophobic surface, and poor adhesion to the matrix, limited overall flexural performance.

For mixtures with higher TA contents, the role of NC was more restricted. When 25% of RS was replaced with TA, the flexural strength increased markedly from 1.64 MPa at 0%NC to 2.36 MPa at 1%NC, and reached 2.57 MPa at 3%NC, equivalent to a 56.7% improvement compared with the baseline. Despite this relative gain, the absolute strength values remained low, and the addition of 5%NC reduced the strength to 1.46 MPa, 43% lower than the optimum. This demonstrates that although NC can improve matrix cohesion, the negative influence of higher TA content-manifested as weak interfacial bonding and increased deformability-dominates the overall flexural response.

The poorest performance was observed in mixtures containing 50%TA. The flexural strength increased only slightly from 0.76 MPa at 0%NC to 0.94 MPa at 1%NC, reaching a maximum of 1.06 MPa at 3%NC, before decreasing to 0.90 MPa at 5%NC. Even at the optimum NC dosage, the strength enhancement was only about 39%, and the final values remained far below those of the RS-only mixtures. This outcome reflects the detrimental role of excessive TA, as the soft and flexible nature of rubber particles prevents effective stress transfer across the ITZ, reduces stiffness, and increases crack propagation under bending loads.

A comparison across mixtures at the optimum 3%NC level highlights the detrimental effect of TA replacement more clearly. While the flexural strength was 4.21 MPa in the control mixture (100%RS), it declined to 2.82 MPa at 10%TA (≈33% reduction), 2.57 MPa at 25%TA (≈39% reduction), and only 1.06 MPa at 50%TA (≈75% reduction). This nearly linear decline emphasizes that rubber aggregates drastically reduce the flexural strength of AACs, regardless of the benefits provided by NC addition. The poor interfacial adhesion of TA with the binder matrix, the presence of voids and micro cracks around rubber particles, and the mismatch in stiffness between TA and the geopolymer matrix are the main causes of this reduction.

The results confirm that NC at moderate contents (around 3%) enhances flexural strength by refining the pore structure, densifying the matrix, and promoting the formation of additional binding gels that improve crack resistance. However, beyond this optimum, the negative effects of NC agglomeration and reduced workability lead to strength losses. Waste tire aggregate, on the other hand, consistently diminishes flexural performance, with greater reductions at higher replacement levels. The best performance was achieved with 100%RS and 3%NC (4.21 MPa), while the worst outcome was observed for 50%RS + 50%TA with 0%NC (0.76 MPa). These findings underline that although NC can significantly improve the bending strength of AACs, its effectiveness is strongly

limited by the presence of rubber aggregates, especially at high replacement ratios. Figure 5b shows a strong correlation ($R^2 = 0.93$) between compressive and flexural strength of AACs. Flexural strength increases with compressive strength up to an optimum and then tends to plateau, indicating that while matrix densification enhances load capacity, crack initiation and weak ITZs limit further flexural gains.

3.3 Oven dry density

Figure 6a provides detailed insight into how NC addition and TA replacement affect the oven-dry density of AACs after thermal curing at 80 °C for 8 h. The reference mix with 100% RS exhibited a baseline density of 1865 kg/m³ at 0% NC. Incorporating 1% NC raised the density to 1940 kg/m³ (+4.0%), and further increasing NC to 3% yielded the highest value of 2022 kg/m³ (+8.4%), confirming that moderate NC levels promote matrix densification. This enhancement is attributed to the dual effect of NC: (i) its ultrafine particles act as fillers that occupy micro voids between binder grains, and (ii) its high surface activity stimulates additional formation of binding gels such as C–(A)–S–H, which consolidates the microstructure. However, when NC reached 5%, density fell sharply to 1776 kg/m³ (−12.2% compared to 3% NC), highlighting the detrimental impact of excessive NC. At high dosages, NC particles tend to agglomerate and significantly increase mix viscosity, reducing workability, entrapping air voids, and creating heterogeneity that compromises compaction efficiency. The effect of TA replacement is equally significant. At constant NC levels, increasing TA from 0% to 50% consistently lowered density due to TA's inherently low specific gravity and porous structure, which introduce more voids into the matrix. For instance, at 0% NC, density decreased from 1865 kg/m³ (0% TA) to 1717 kg/m³ (50% TA), a 7.9% reduction. Similarly, at 3% NC, the decrease was from 2022 kg/m³ to 1790 kg/m³ (−11.5%). Even though NC addition partially mitigates this negative effect by refining the microstructure and improving paste-aggregate bonding, it cannot fully counteract the high porosity introduced by TA. Furthermore, the combination of excessive NC (5%) and high TA (50%) amplifies these issues, yielding a structurally less compact matrix and the lowest observed density trend within the set of mixes.

Overall, the data suggest that a balanced NC content of approximately 3% is optimal for achieving maximum density, while maintaining TA at lower replacement levels helps preserve structural integrity. The densest mix was 100% RS with 3% NC (2022 kg/m³), reflecting superior packing and gel development, whereas the most porous system was 50% TA with 0% NC (1717 kg/m³), which suffered from both aggregate porosity and lack of microstructural refinement. These findings underscore the importance of optimizing NC dosage in conjunction with TA content to enhance density, which directly correlates with improved mechanical strength, lower

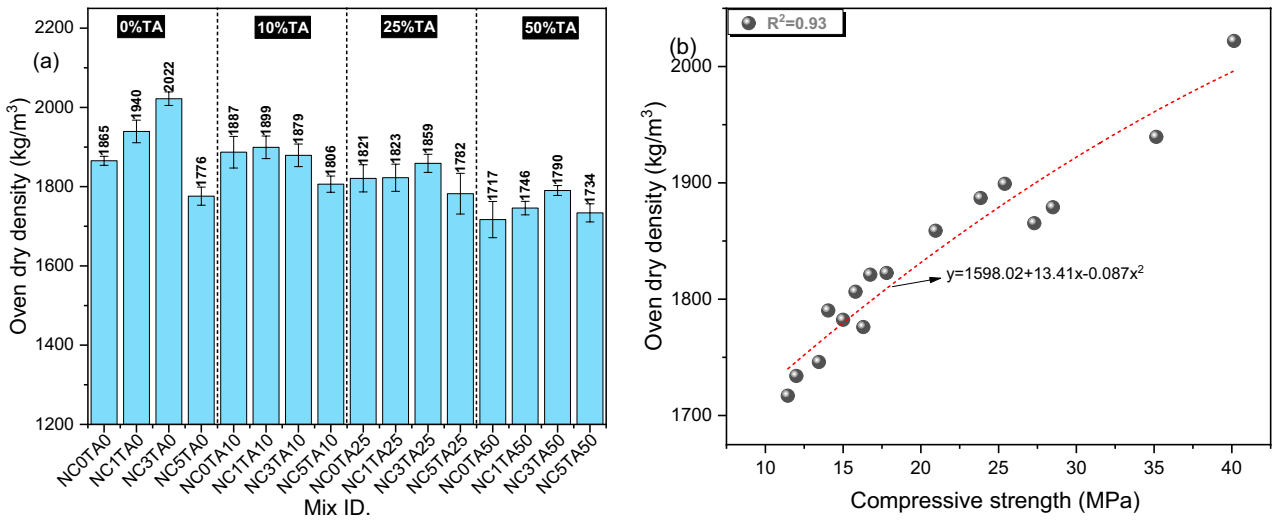


Fig. 6 **a** Variation in oven-dry density of AAC mixtures; **b** Correlation between compressive strength and dry density

permeability, and superior durability performance in AAC systems. Figure 6b shows a strong positive correlation ($R^2 = 0.93$) between oven-dry density and compressive strength of AACs, indicating density is a reliable predictor of mechanical performance. Higher density corresponds to reduced porosity and better particle packing, which promotes a continuous gel network and improves stress transfer. Conversely, lower density—often linked to higher TA content and/or excessive NC—results in weaker strength due to increased voids and poor interfacial bonding. This trend highlights the importance of optimal NC dosage (≈3%) and limited TA replacement to achieve a dense, homogeneous structure for maximum strength and durability.

3.4 The porosity and water absorption

Figure 7a illustrates the combined effects of NC addition, used as a partial replacement for GBFS, and RS substitution with TA on the porosity of AACs subjected to thermal curing at 80 °C for 8 h. The results reveal a clear interaction between NC and TA: while moderate NC contents (1–3%) generally reduce porosity through microstructural refinement, excessive NC (5%) reverses this trend and significantly increases porosity due to agglomeration and higher water demand. TA replacement, on the other hand, consistently elevates porosity across all NC levels, owing to its low density, hydrophobic surface, and weak interfacial bonding with the binder matrix.

For the reference mixture with 100%RS (0%TA), porosity decreased progressively from 8.84% at 0%NC to 7.65% at 1%NC, corresponding to a ≈ 13.5% reduction. At 3%NC, porosity further dropped to 6.79%, which represents a ≈ 23% reduction compared with the unmodified mix and marks the lowest porosity among all mixtures. This improvement indicates that small additions of NC enhance gel formation (C–(A)–S–H and N–A–S–H phases) [71], refine pore structure [72], and increase compactness [73]. However, when NC content reached 5%, porosity rose sharply to 11.26%, a ≈ 65.8% increase compared to the 3%NC mix. This reversal can be explained by the excessive fineness and platelet morphology of NC, which promotes water absorption, reduces workability, and generates micro defects and weak zones, leading to a more porous microstructure [74].

The mixture with 90%RS + 10%TA exhibited a slightly different trend. Porosity initially increased from 8.10% at 0%NC to 9.08% at 1%NC (≈12% rise), then decreased slightly to 8.51% at 3%NC (≈6% reduction relative to 1%NC), before rising again to 10.86% at 5%NC (≈27.6% increase compared with 3%NC). These results suggest that the weak bonding and voids introduced by TA particles limited the beneficial effects of NC. Although 3%NC

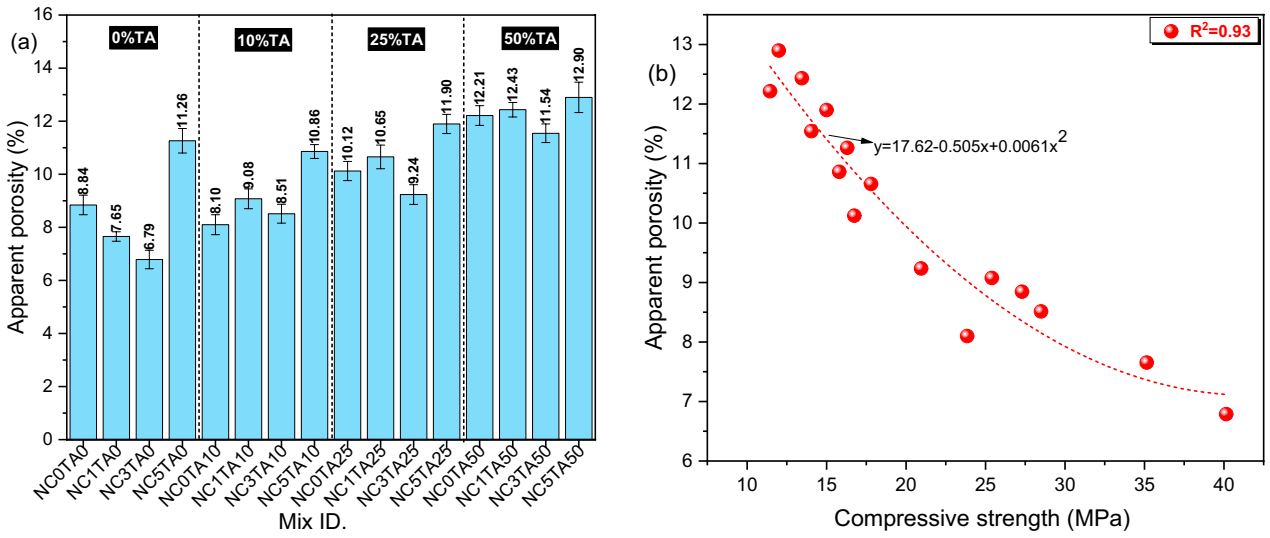


Fig. 7 **a** Changes in apparent porosity and water absorption across different AAC mixtures; **b** correlation between porosity and compressive strength

offered some refinement, the reduction in porosity was not as significant as in the 100%RS mixture, confirming that the presence of rubber aggregates diminishes the efficiency of NC in densifying the matrix.

In the 75%RS + 25%TA mixture, porosity followed a similar pattern but at generally higher values. It was measured at 10.12% for 0%NC, increased slightly to 10.65% at 1%NC (≈5.2% rise), then decreased to 9.24% at 3%NC (≈13.2% reduction compared to 1%NC), before climbing again to 11.90% at 5%NC (≈28.7% increase from 3%NC). These results show that although NC at 3% could partially densify the matrix, the dominant effect of TA-through its elastic and porous nature-kept porosity values relatively high compared to the RS-only series. The sharp rise at 5%NC once again reflects the negative influence of excessive NC content.

The highest porosity values were observed in the 50%RS + 50%TA mixture. Porosity increased from 12.21% at 0%NC to 12.43% at 1%NC (≈1.8% increase), decreased slightly to 11.54% at 3%NC (≈7.2% reduction compared to 1%NC), and then increased again to 12.90% at 5%NC (≈11.8% increase from 3%NC). These findings emphasize that at high TA replacement levels, the effect of NC is very limited, since the pore structure is primarily governed by the lightweight, porous rubber aggregates and their poor adhesion with the geopolymer matrix. Even the slight porosity reduction at 3%NC could not offset the dominant influence of TA, and porosity quickly rose again at 5%NC.

Taken together, the results confirm several key trends: At 1–3%NC, porosity decreases due to enhanced geopolymerization and gel formation, producing denser and more refined microstructures. At 5%NC, however, porosity rises sharply in all mixtures, highlighting the negative impact of excessive NC content.

TA consistently increases porosity, with baseline values rising from 8.84% at 0%TA to 12.21% at 50%TA (≈38% increase). This is attributed to TA's low specific gravity, irregular and porous structure, and hydrophobic surface, which hinder proper matrix compaction and promote void formation.

The lowest porosity (6.79%) was achieved in the 100%RS + 3%NC mixture, confirming the optimal role of moderate NC dosage in pore refinement. Conversely, the highest porosity (12.90%) was observed in the 50%RS + 50%TA + 5%NC mixture, where both high TA content and excessive NC acted synergistically to increase void content.

these findings suggest that the best balance between porosity control and lightweight performance can be achieved by using moderate NC dosages (1–3%) in mixtures with low to moderate TA replacement (≤25%). Excessive NC (5%) and high TA contents (50%) should be avoided, as they result in substantial porosity increases, which can negatively affect durability and mechanical performance despite reducing density. Figure 7b shows the inverse correlation between porosity and compressive strength, with higher porosity leading to lower strength ($R^2 = 0.93$).

Figure 8a illustrates the effect of NC incorporation (0, 1, 3, and 5% as a partial replacement for GBFS and RS substitution with TA on the water absorption of AACs cured at 80 °C for 8 h. The results demonstrate that NC and TA influence water uptake in opposite ways: NC at moderate levels (1–3%) reduces water absorption through microstructural refinement, while excessive NC (5%) increases absorption due to agglomeration, higher water demand, and pore formation; TA replacement consistently raises absorption because of its low density, porous structure, and weak adhesion at the interfacial transition zone (ITZ).

For the control mixture with 100%RS (0%TA), absorption decreased from 7.32% at 0%NC to 6.55% at 1%NC (≈10.5% reduction) and further to 5.35% at 3%NC (≈26.9% reduction), but then increased sharply to 9.22% at 5%NC (≈72% rise compared with 3%NC). In the 90%RS + 10%TA mix, absorption rose slightly from 6.85% at 0%NC to 7.65% at 1%NC (≈11.7% increase), decreased to 6.87% at 3%NC (≈10% reduction compared with 1%NC), and increased again to 8.85% at 5%NC (≈29% increase relative to 3%NC). For the 75%RS + 25%TA mixture, absorption followed a similar pattern: 8.26% at 0%NC, 8.35% at 1%NC (≈1% rise), 7.78% at 3%NC (≈7% reduction compared with 1%NC), and 9.70% at 5%NC (≈25% increase compared with 3%NC). The highest absorption values were obtained in the 50%RS + 50%TA mixtures, where absorption increased from 10.23% at 0%NC to 10.43% at 1%NC (≈2% increase), decreased to 9.13% at 3%NC (≈12.5% reduction compared with 1%NC), and then increased to 10.88% at 5%NC (≈19% increase compared with 3%NC).

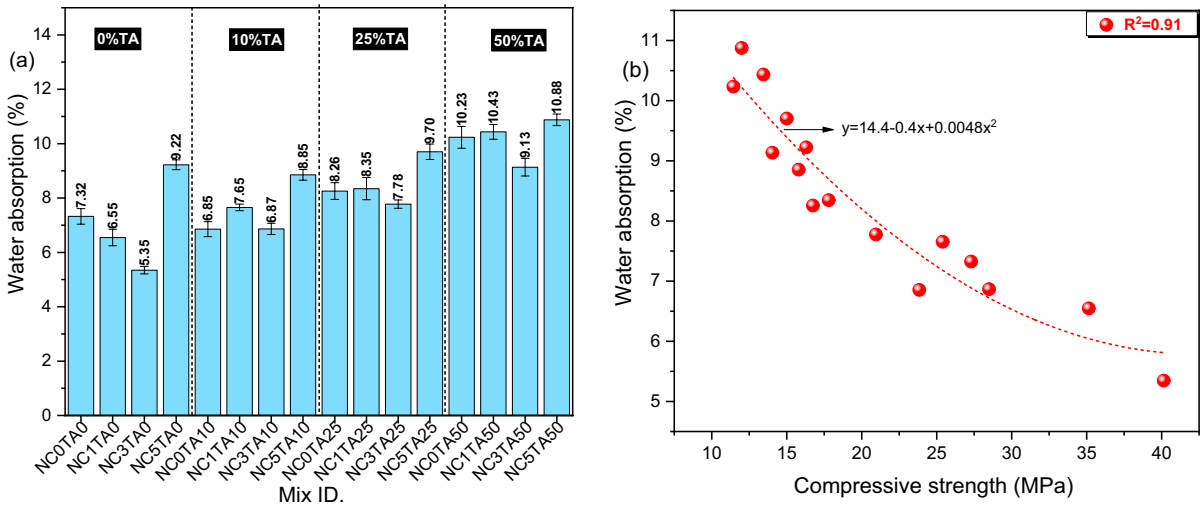


Fig. 8 **a** Changes in water absorption across different AAC mixtures; **b** correlation between water absorption and compressive strength

At moderate levels (1–3%), NC effectively reduces water absorption by improving matrix densification [73] and refining pore connectivity, with reductions as high as ≈ 27% in the control mixture [75]. However, at 5%NC, absorption increases in all mixtures (≈ 20–70% higher compared with the 3%NC level), confirming that excessive NC is detrimental to microstructural integrity. Increasing TA consistently raises water absorption at every NC level. For example, at 0%NC, absorption increases from 7.32% (0%TA) to 10.23% (50%TA), a ≈ 40% rise. This effect stems from TA's porous and elastic characteristics, which reduce compactness and generate pathways for water ingress [76]. The best-performing mix was the 100%RS + 3%NC composition, which exhibited the lowest water absorption (5.35%), reflecting an optimal balance of matrix densification and reduced permeability [77]. In contrast, the worst-performing mix was the 50%RS + 50%TA + 5%NC composition, which showed the highest water absorption (10.88%), where the combination of high TA content and excessive NC resulted in a highly porous structure prone to fluid penetration [78].

These findings highlight that moderate NC dosages in combination with limited TA content can optimize pore structure and minimize water absorption, whereas excessive NC and higher TA replacement lead to porous, permeable composites that may compromise durability under aggressive environmental exposure. Figure 8b shows a strong negative correlation ($R^2 = 0.91$) between water absorption and compressive strength of AACs. Low absorption (≈5–7%) at 1–3% NC corresponds to higher strength due to matrix densification, while higher absorption (≈8–11%) from excess NC or TA leads to lower strength through increased porosity and weaker ITZ.

3.5 Sorptivity

Sorptivity represents a material's capacity to absorb water via capillary action [79]. It is an essential indicator of the durability of cementitious composites [80], as higher sorptivity signifies increased susceptibility to moisture penetration [81], which can accelerate deterioration processes such as freeze–thaw damage [82], chemical attack [83], and reinforcement corrosion [84].

Figure 9a illustrates the effect of NC) addition (0, 1, 3, and 5% as a partial replacement of GBFS and RS substitution with TA on the sorptivity of AACs cured at 80 °C for 8 h. The results show that NC and TA strongly influence the capillary suction behavior of AACs. For the control mixture with 100%RS (0%TA), sorptivity decreased from 1.90 at 0%NC to 1.66 at 1%NC (≈ 12.6% reduction) and further to 1.27 at 3%NC (≈ 33.2% reduction), indicating effective pore refinement [76] and matrix densification [85]. However, at 5%NC sorptivity rose sharply to 2.46 (≈ 93.7% higher than 3%NC), showing that excessive NC leads to agglomeration and

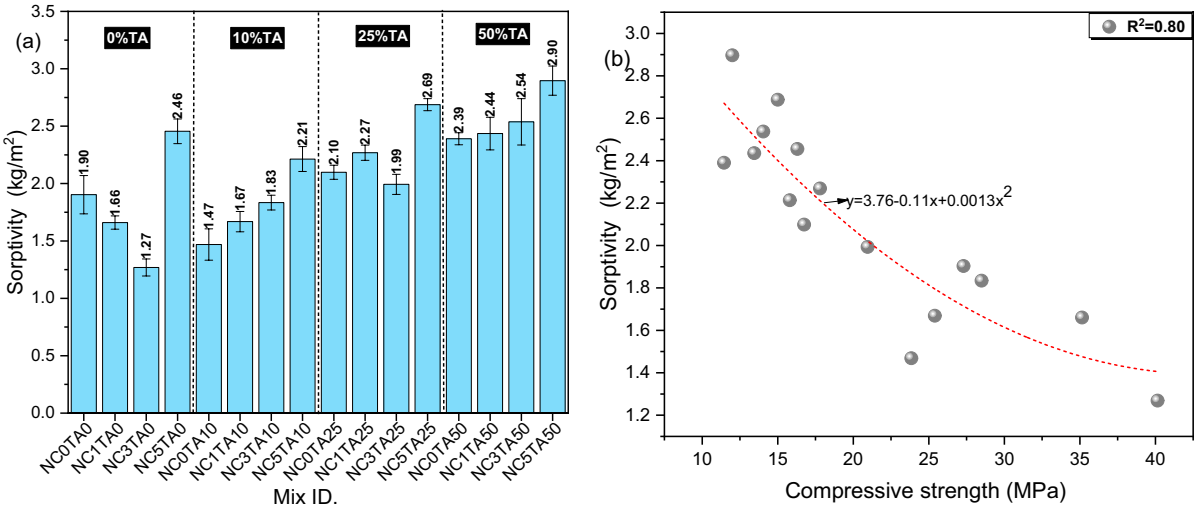


Fig. 9 **a** Effect of mix composition on sorptivity; **b** relationship between sorptivity and compressive strength

increased porosity. In the 90%RS + 10%TA mixture, sorptivity values increased steadily from 1.47 at 0%NC to 1.67 at 1%NC (≈ 13.6% rise), 1.83 at 3%NC (≈ 24.5% increase), and 2.21 at 5%NC (≈ 50.3% increase compared to 0%NC), suggesting that the presence of TA reduced the effectiveness of NC and promoted water transport. For the 75%RS + 25%TA series, sorptivity rose from 2.10 at 0%NC to 2.27 at 1%NC (≈ 8.1% increase), decreased to 1.99 at 3%NC (≈ 12.3% reduction compared with 1%NC), and then increased again to 2.69 at 5%NC (≈ 35.2% increase relative to 3%NC). This indicates that while 3%NC could partially improve microstructure, TA's porous and weak ITZ properties remained dominant [78]. In the 50%RS + 50%TA mixture, the highest sorptivity values were observed, rising from 2.39 at 0%NC to 2.44 at 1%NC (≈ 2.1% increase), 2.54 at 3%NC (≈ 6.3% increase), and 2.90 at 5%NC (≈ 21.4% increase compared to baseline).

In TA-free mixes, NC at 1–3% substantially reduced sorptivity (up to ≈ 33%), confirming its role in densifying the matrix and refining pore structure. However, at 5%NC sorptivity increased significantly in all mixes (up to ≈ 94% higher compared to the 3%NC control), showing that excessive NC promotes microstructural defects and increased capillary suction. TA consistently raised sorptivity at all NC levels. For instance, at 0%NC, sorptivity increased from 1.90 (0%TA) to 2.39 (50%TA), representing a ≈ 26% increase. At 5%NC, the difference became more severe, with sorptivity values rising from 2.46 (0%TA) to 2.90 (50%TA). The best-performing mixture was the 100%RS + 3%NC composition, which achieved the lowest sorptivity (1.27), indicating optimal pore refinement [71] and reduced capillary absorption [76]. In contrast, the worst-performing mixture was the 50%RS + 50%TA + 5%NC composition, which exhibited the highest sorptivity (2.90), where the combined effect of high TA content and excessive NC resulted in a highly porous and permeable structure. These findings emphasize that moderate NC dosages provide pore refinement and durability benefits, whereas excessive NC and higher TA levels synergistically increase sorptivity, thereby compromising long-term durability by facilitating rapid water ingress. Figure 9b shows a clear inverse relationship ($R^2 = 0.80$) between sorptivity and compressive strength. Lower sorptivity, achieved with 1–3% NC in TA-free mixes, corresponds to higher strength due to refined pore structure. In contrast, higher sorptivity from excessive NC (5%) or TA addition leads to strength loss, confirming that increased pore connectivity weakens the matrix.

3.6 Microstructural changes

3.6.1 SEM observations

Figure 10a presents the SEM microstructural features of the NC1TA10 mixture (1% NC, 10% TA, cured at 80 °C for 8 h), which achieved a compressive strength of 25.40 MPa. The SEM micrographs of the NC1TA10 mixture reveal a heterogeneous but moderately consolidated matrix, in which both beneficial and detrimental microstructural features coexist. Distinct lamellar and plate-like NC sheets are discernible within the alkali-activated binder phase. These NC particles act as nucleation sites and locally refine the pore structure, yet their incomplete dispersion results in clustered domains, limiting the overall efficiency of pore refinement across the matrix.

The interfacial transition zone (ITZ) surrounding TA particles is notably weak and porous. SEM observations show micro cracked and rough boundaries, consistent with the non-polar, hydrophobic nature of rubber and the absence of chemical compatibility with the alkali-activated binder. This poor ITZ quality facilitates micro-void development and crack initiation, serving as preferential sites for durability degradation [86].

In contrast, C-(A)-S-H type gels appear as dense but discontinuous phases coating the surfaces of angular slag grains. These gels contribute to localized densification, although their non-uniform distribution leads to zones of variable stiffness and strength. Several micro-cracks are visible throughout the matrix, intersecting both gel and unreacted slag phases, which are likely linked to autogenous shrinkage, stress concentration around TA inclusions, and curing-induced thermal gradients.

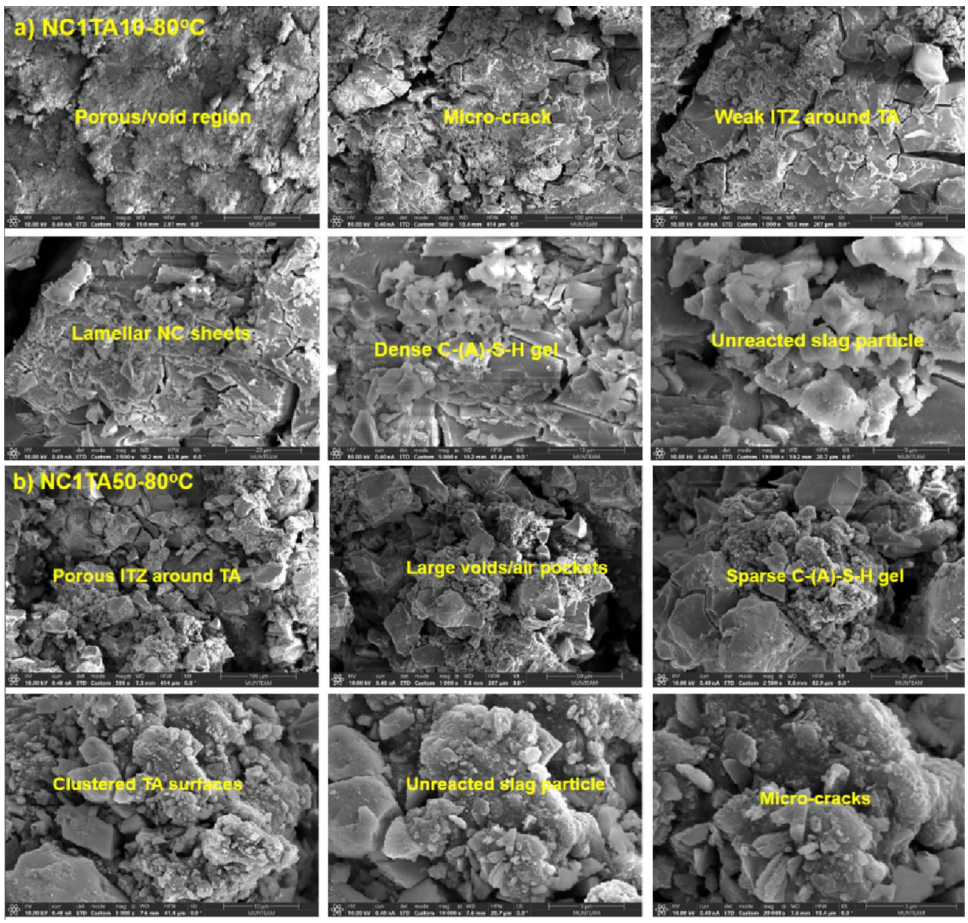


Fig. 10 Microstructures of specimens after 80 °C curing **a** NC1TA10-80 °C **b** NC1TA50-80 °C

The microstructure also exhibits porous regions and entrapped voids, reflecting incomplete particle packing and viscosity-related air entrapment. Moreover, occasional unreacted slag particles embedded in the gel phase further confirm incomplete geopolymerization under the adopted curing regime.

These combined features provide a mechanistic explanation for the moderate compressive strength (25.40 MPa) recorded for NC1TA10. While nano-clay contributes to gel nucleation, microstructural densification, and improved packing, the incorporation of TA introduces structural discontinuities, weak ITZ bonding, and additional porosity. This dual effect highlights the delicate balance between sustainability-driven aggregate replacement and mechanical performance in alkali-activated systems.

Figure 10b presents the SEM microstructural features of the NC1TA50 mixture (1% NC, 50% TA, cured at 80 °C for 8 h), which reached a compressive strength of only 13.45 MPa. The matrix is characterized by a highly porous and heterogeneous morphology, with extensive weak zones formed around the tire aggregate particles. The substitution of half of the natural sand with TA markedly disrupted the packing density and created porous interfacial transition zones (ITZs), where poor gel adhesion and micro-cracks are evident. The hydrophobic and chemically inert nature of rubber particles further hindered bonding, resulting in clustered TA surfaces surrounded by loose reaction products.

Compared to NC1TA10, the C–(A)–S–H gels [87] in NC1TA50 are less abundant, thinner, and discontinuous, leaving many unreacted slag grains embedded within the matrix. The presence of large voids, entrapped air pockets, and extensive micro-cracking dominates the microstructure, severely impairing matrix continuity and mechanical performance. These combined features explain the sharp decline in compressive strength, demonstrating that at high TA contents, the limited nucleation effect of NC cannot overcome the detrimental influence of rubber inclusion. The SEM observations thus corroborate the macroscopic strength results, highlighting the microstructural incompatibility introduced by excessive TA replacement.

3.6.2 EDS results

Figure 11a presents the SEM and EDS analyses of the NC1TA10 mixture (1% NC, 10% TA) after thermal curing at 80 °C for 8 h. This mixture achieved a compressive strength of 25.40 MPa. SEM observations reveal a relatively compact matrix with lamellar NC sheets uniformly embedded within the alkali-activated binder, promoting

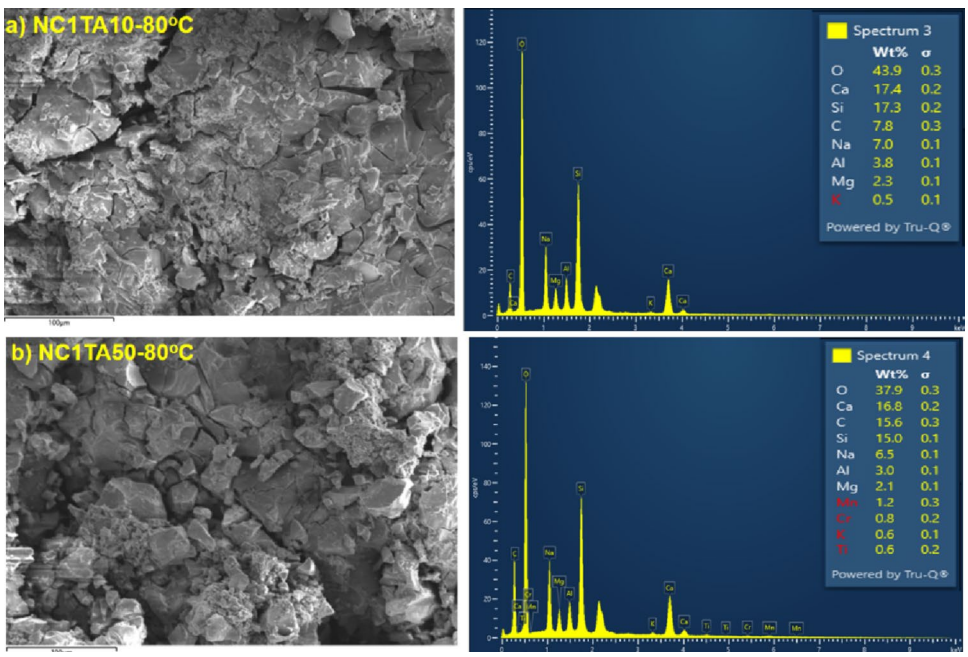


Fig. 11 EDS results of specimens after 80 °C curing **a** NC1TA10-80 °C **b** NC1TA50-80 °C

local pore refinement and matrix densification. Nevertheless, isolated micro-cracks and porous ITZs remain visible around the tire aggregate due to its hydrophobic nature and weak adhesion. EDS analysis is dominated by oxygen (43.9 wt%), calcium (17.4 wt%), and silicon (17.3 wt%), confirming the formation of C-(A)-S-H gels as the primary binding phase. Sodium (7.0 wt%) and aluminum (3.8 wt%) indicate effective alkali activation, while magnesium (2.3 wt%) suggests the presence of hydrotalcite-like secondary products. The carbon signal (7.8 wt%) reflects the incorporation of tire aggregate. Overall, the relatively dense microstructure explains the moderate compressive strength, although the weak ITZ around the rubber particles limits further improvement.

Figure 11b shows the SEM and EDS analyses of the NC1TA50 mixture (1% NC, 50% TA), which exhibited a compressive strength of 13.45 MPa. A highly porous and discontinuous matrix with abundant voids, extensive micro-cracking, and poorly bonded ITZs is evident. Compared with NC1TA10, the gel network is fragmented and discontinuous, while numerous unreacted slag particles remain embedded within the matrix. EDS results, characterized by oxygen (37.9 wt%), calcium (16.8 wt%), silicon (15.0 wt%), sodium (6.5 wt%), and aluminum (3.0 wt%), confirm the presence of C-(A)-S-H gels but indicate a less developed reaction product network. The markedly higher carbon content (15.6 wt%) reflects the greater proportion of tire aggregate and its limited interaction with the binder.

Comparison of the two mixtures demonstrates that increasing TA content from 10% to 50% substantially reduces matrix continuity and gel development. While NC1TA10 exhibits a relatively dense binder with localized pore refinement provided by NC, NC1TA50 is dominated by porous ITZs, fragmented gels, and abundant voids associated with the high rubber content. The higher carbon signal and poorer matrix continuity observed in NC1TA50 explain its significantly lower compressive strength. These results indicate that excessive TA content outweighs the beneficial pore-refining effect of NC, leading to reduced mechanical performance.

3.7 High-temperature durability performance of AACs

3.7.1 Compressive strength

Figure 12a illustrates the compressive strength of AACs cured at 80 °C for 8 h and subsequently exposed to elevated temperatures of 200 °C, 400 °C, and 600 °C, while Fig. 12b presents the corresponding strength losses. The thermal behavior of the mixtures can be interpreted within three distinct regimes governed by different dominant mechanisms.

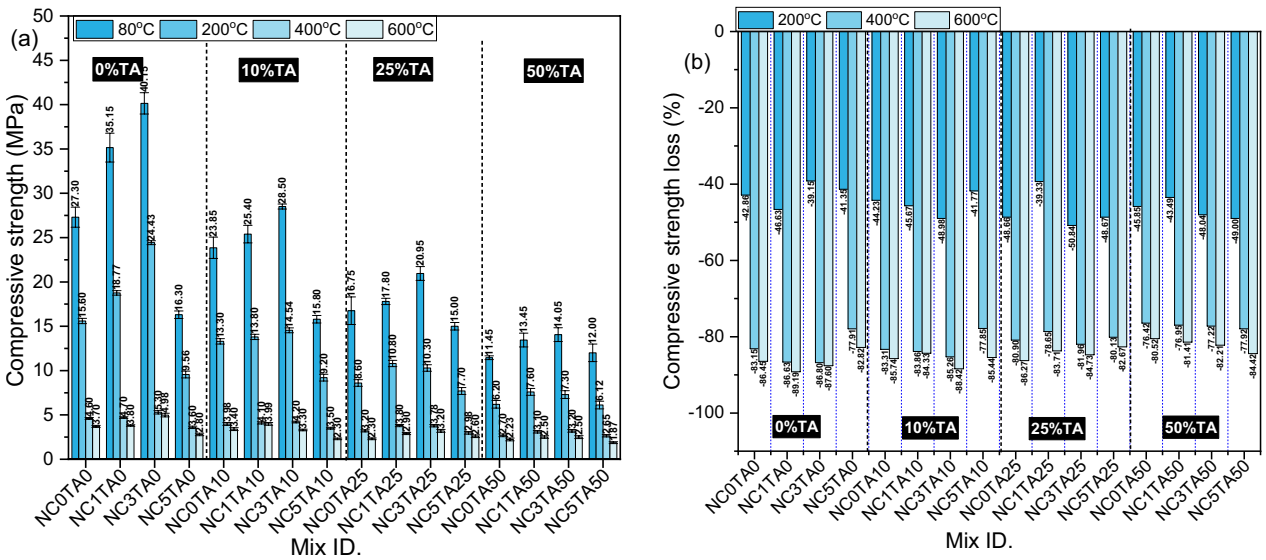


Fig. 12 **a** Compressive strength at elevated temperatures; **b** associated strength loss due to thermal exposure

At lower temperatures (≤ 200 °C), compressive strength losses ranged from approximately 39% to 51% across all mixtures, reflecting initial microstructural degradation associated with moisture evaporation and early-stage gel modification. In this regime, performance is primarily governed by matrix densification and gel stability [88]. The 100% RS mixture with 3% NC exhibited the lowest strength loss (39.15%), confirming that NC enhances thermal resistance by refining pore structure [33] and promoting the formation of stable C–(A)–S–H and N–A–S–H gels [89]. However, in mixtures with higher TA content (≥ 25%), such as the 75% RS + 25% TA system, the beneficial effect of NC became less pronounced, likely due to weakened ITZs and reduced matrix cohesion caused by the hydrophobic and deformable nature of tire aggregates.

At intermediate temperatures (~ 400 °C), strength losses increased significantly to approximately 76–87%, indicating severe degradation driven by dehydration of gel phases, matrix shrinkage [90], and thermal incompatibility between binder and aggregates [91]. In this regime, the role of TA becomes more prominent. The mixture containing 50% TA exhibited the lowest strength loss (≈ 76%), demonstrating that the porous and deformable nature of tire particles provides an effective stress-relief mechanism by accommodating thermal strains and reducing crack propagation. In contrast, mixtures dominated by RS showed higher losses (> 80%), reflecting the brittle response of a dense matrix with limited strain accommodation capacity [92]. Although NC contributes to pore refinement and gel formation at lower temperatures, its influence diminishes at this stage as progressive gel dehydration and structural instability become dominant.

At high temperature (600 °C), nearly all mixtures experienced catastrophic strength losses exceeding 80–89%, indicating complete degradation of the binder matrix. This behavior is primarily governed by the dehydration and breakdown of C–(A)–S–H and N–A–S–H gels, leading to pore coarsening, micro crack propagation, and loss of structural continuity [93]. The corresponding weight loss values (up to approximately 27%) are directly associated with gel decomposition and explain the severe reduction in compressive strength. Although no quantitative spalling measurements were conducted, visual observations during thermal exposure indicated reduced surface spalling in TA-containing mixtures. This behavior can be attributed to the lower stiffness and stress-relief capacity of rubber particles; however, this observation remains qualitative and requires further investigation.

Despite the overall degradation at 600 °C, mixtures with higher TA content (≈50%) showed relatively lower strength loss (≈80–84%), highlighting the thermal buffering capacity of tire aggregates through energy absorption and deformation. In contrast, RS-dominant mixtures exhibited more pronounced cracking and higher losses (>89%) due to thermal incompatibility and brittle failure.

The results demonstrate that thermal resistance of AACs is governed by a transition from densification-controlled behavior at low temperatures to stress accommodation at intermediate temperatures, and finally to gel-decomposition-dominated failure at high temperatures. These findings confirm that the combined use of NC and TA provides a complementary mechanism, where NC enhances matrix stability at lower temperatures, while TA improves resistance to thermally induced stresses at elevated temperatures.

3.7.2 Weight loss

Figures 13a presents the thermal weight loss characteristics of alkali-activated composites (AACs) after exposure to 200 °C, 400 °C, and 600 °C, providing critical insights into the thermal stability and degradation mechanisms of mixes containing different proportions of river sand (RS), tire aggregate (TA), and nano-clay (NC). At 200 °C, weight losses were relatively minor, ranging between 5.0% and 7.6% across all mixtures, which primarily corresponds to the evaporation of physically adsorbed water and loosely bound moisture within the gel pores. The magnitude of weight loss at this stage reflects the initial porosity of the matrix: TA-rich systems (e.g., 50% TA) exhibited the highest weight losses (≈ 7.55–7.43%), owing to the high surface area and interconnected voids associated with the inclusion of rubber particles, which facilitated water retention during curing. Conversely, mixes with higher RS content and moderate NC incorporation (e.g., 3% NC in 100% RS mix) recorded the lowest losses (≈ 5.04%), demonstrating the densifying effect of NC due to its fine particle size, filler action, and contribution to additional gel formation that reduces capillary water availability [94].

 https://doi.org/10.1007/s43452-026-01614-2

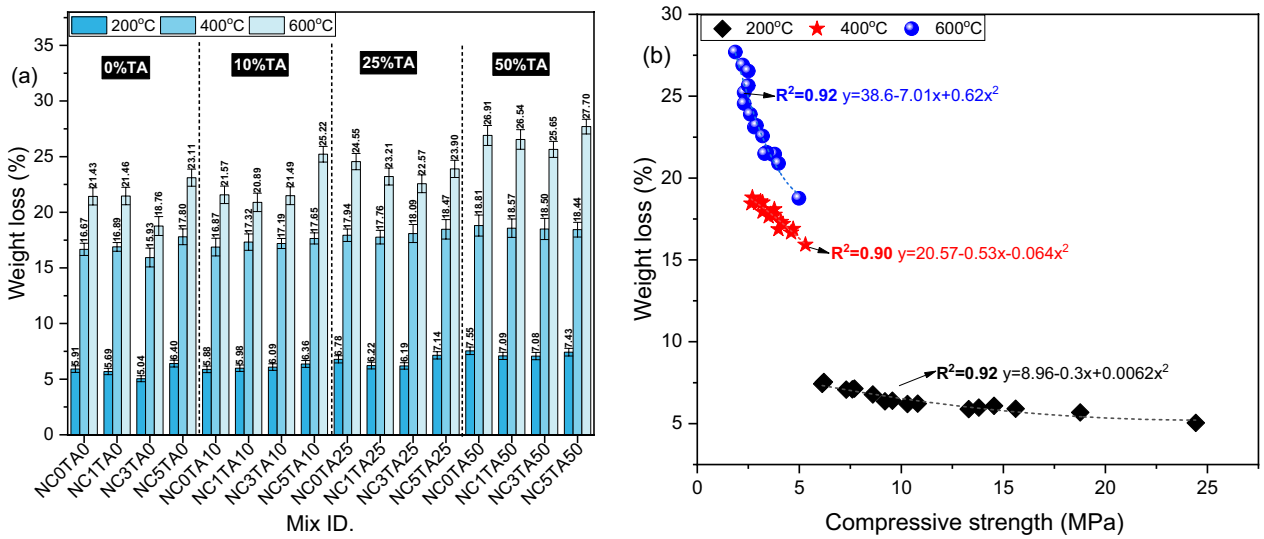


Fig. 13 **a** Weight loss of the mixtures cured under high temperatures **b** compressive strength versus weight loss

As the temperature increased to 400 °C, weight loss rose markedly to 16.7–18.8%, indicating the release of chemically bound water from the N–A–S–H and C–(A)–S–H gel phases, accompanied by partial carbonate decomposition and disruption of the aluminosilicate network. This critical dehydration stage initiated matrix shrinkage, micro-cracking, and the deterioration of mechanical integrity. Mixtures containing 3% NC consistently exhibited slightly lower weight losses than NC-free mixtures, indicating improved gel cohesion and reduced pore connectivity. In contrast, TA-rich mixtures recorded the highest weight losses (up to 18.81%) because their higher porosity and thermal incompatibility promoted internal stress development during heating. These observations demonstrate that progressive gel dehydration is the primary mechanism responsible for the onset of thermal degradation.

At 600 °C, weight loss further increased to 21–28%, reflecting complete dehydration of the binding gels, decomposition of residual hydrates, and collapse of the pore structure. Thermal softening and partial pyrolysis of the tire aggregate generated additional voids and released volatile compounds, further weakening the matrix. The 50% TA mixture without NC exhibited the highest weight loss (27.7%), confirming the poor thermal stability of rubber-rich systems. Although NC continued to provide limited stabilization by improving gel cohesion, its beneficial effect became negligible at this temperature. The pronounced increase in weight loss closely corresponded to the severe reduction in compressive strength, confirming that degradation of the gel network governed both mass loss and mechanical deterioration.

The thermal stability of AACs was primarily controlled by the exposure temperature and TA content. Moderate NC addition improved microstructural stability at temperatures up to 400 °C, whereas its effectiveness diminished under severe thermal exposure. Although TA reduced thermal conductivity and mitigated explosive spalling, excessive TA increased mass loss and structural instability above 400 °C, indicating that both NC dosage and TA replacement level should be carefully optimized for high-temperature applications. As shown in Fig. 13b, weight loss and compressive strength exhibited a strong inverse correlation ($R^2 > 0.90$), demonstrating that both properties are governed by the same degradation mechanism involving gel decomposition and microstructural collapse.

3.7.3 Microstructural changes after 600 °C

Figure 14a shows the SEM microstructure of the NC1TA0 mixture (1% NC, 100% RS, 0% TA) after exposure to 600 °C. This mixture exhibited the greatest compressive strength loss (89.19%), indicating severe thermal

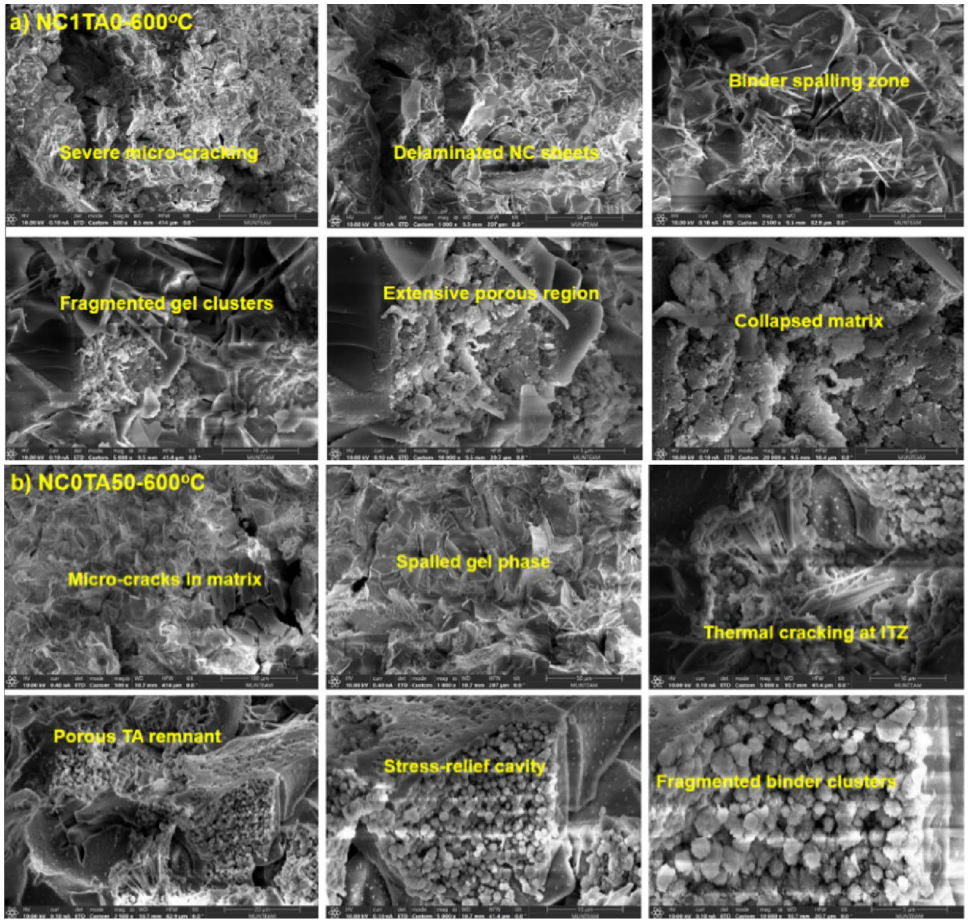


Fig. 14 Microstructural characteristics after exposure to 600 °C **a** NC1TA0-600 °C **b** NC0TA50-600 °C

degradation. SEM observations reveal extensive micro-cracking, matrix spalling, and fragmentation of the binder gel, resulting in a highly porous and discontinuous microstructure. The originally dense C–(A)–S–H gel network collapsed because of dehydration and shrinkage, while the lamellar NC sheets became distorted and delaminated under elevated temperature. In the absence of tire aggregate, no stress-relief mechanism was available to accommodate thermal expansion, leading to brittle fracture and catastrophic matrix collapse. These observations explain the severe deterioration in mechanical performance and confirm that gel dehydration and microstructural collapse are the primary mechanisms governing both mass loss and strength reduction at high temperature.

Figure 14b presents the SEM microstructure of the NC0TA50 mixture (100% GBFS, 50% TA) after exposure to 600 °C. Although this mixture also underwent considerable degradation, it exhibited the lowest compressive strength loss (80.52%) among all mixtures. SEM images reveal a cracked and porous matrix with fragmented gel phases and surface spalling. However, the porous cavities left by thermally degraded TA acted as stress-relief zones that accommodated thermal expansion and reduced crack severity [95]. Although the absence of NC limited matrix densification, the softening and partial pyrolysis of TA reduced brittle failure and prevented complete structural collapse. Consequently, despite the increased porosity, the TA-rich mixture exhibited greater tolerance to thermal damage than the TA-free system. The SEM observations demonstrate that the thermal performance of AACs is governed by gel dehydration and microstructural degradation. While NC1TA0 failed through extensive gel collapse and brittle fracture, NC0TA50 benefited from the strain-accommodating effect of TA, which alleviated thermal stresses and limited crack propagation, resulting in comparatively better residual performance.

Figure 15a presents the SEM and EDS analyses of the NC1TA0 mixture (99% GBFS, 1% NC, 100% RS, 0% TA) after curing at 80 °C for 8 h and subsequent exposure to 600 °C. This mixture exhibited the greatest compressive strength loss (89.19%), indicating severe thermal degradation. SEM observations reveal extensive

 https://doi.org/10.1007/s43452-026-01614-2

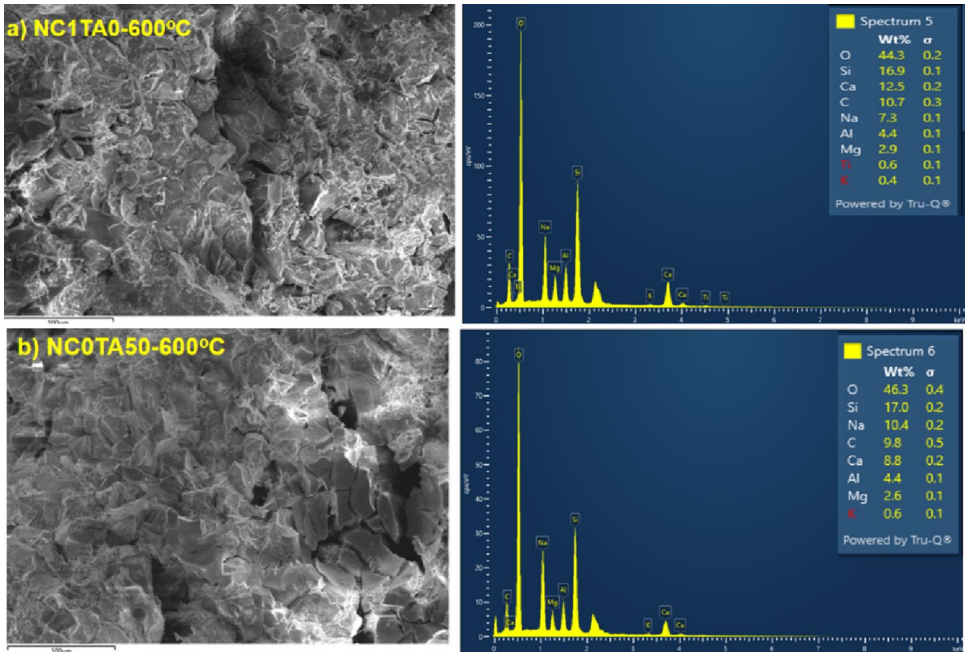


Fig. 15 EDS results after exposure to 600 °C **a** NC1TA0-600 °C **b** NC0TA50-600 °C

micro-cracking, binder spalling, gel decomposition, and a highly porous, fragmented matrix. The lamellar NC structure became distorted and delaminated, while the absence of TA prevented stress redistribution, resulting in brittle failure. EDS analysis identified oxygen (44.3 wt%), silicon (16.9 wt%), calcium (12.5 wt%), sodium (7.3 wt%), and aluminum (4.4 wt%), confirming the degradation of C-(A)-S-H gels and partial retention of alkali-activated phases. Magnesium (2.9 wt%) indicates residual hydrotalcite-like products, whereas the elevated carbon content (10.7 wt%) is attributed to carbonation or minor contamination. These observations explain the severe matrix collapse and the corresponding loss in mechanical performance.

Figure 15b presents the SEM and EDS analyses of the NC0TA50 mixture (100% GBFS, 50% RS, 50% TA) after exposure to 600 °C. Although this mixture also exhibited substantial deterioration, it showed the lowest compressive strength loss (80.52%) among the tested mixtures. SEM images reveal a cracked and porous matrix with decomposed gel products, while the cavities left by thermally degraded TA acted as stress-relief zones that reduced crack propagation and mitigated brittle failure. EDS results, dominated by oxygen (46.3 wt%), silicon (17.0 wt%), calcium (8.8 wt%), sodium (10.4 wt%), and aluminum (4.4 wt%), indicate degraded C-(A)-S-H gels together with residual alkali-aluminosilicate phases. The relatively high carbon content (9.8 wt%) confirms the presence of pyrolyzed TA. Although TA increased porosity, it also improved the composite's relative resistance to thermal shock by accommodating thermal strain.

Comparison of the two mixtures shows that NC1TA0 underwent severe gel decomposition and brittle matrix collapse because no stress-relief mechanism was available. In contrast, NC0TA50 developed internal cavities following TA degradation, which alleviated thermal stresses and limited crack propagation. Consequently, despite its lower ambient-temperature performance, the TA-containing mixture exhibited better residual thermal stability than the TA-free mixture.

4 Exposure to $MgSO_4$

4.1 The compressive strength

Figure 16a presents the evolution of compressive strength of AACs cured at 80 °C and subjected to 5% $MgSO_4$ solution for 120 days, while Fig. 16b illustrates the corresponding percentage losses in compressive strength. The results clearly demonstrate that both NC addition and TA replacement significantly influence the sulfate resistance of AACs, primarily through their effects on matrix densification, pore connectivity, and interfacial transition zones.

For the control mix containing 100% RS and no TA, the compressive strength loss after sulfate exposure decreased progressively from 14.54% at 0% NC to 9.84% at 1% NC and further to 6.33% at 3% NC, reflecting the positive role of moderate NC dosages in refining pore structure and blocking sulfate ingress [28]. This improvement can be attributed to the formation of additional binding gels, primarily C–(A)–S–H and some N–A–S–H [96], along with reduced capillary porosity due to the filler effect and surface reactivity of NC, which enhances matrix densification [97]. However, at 5% NC, the strength loss sharply increased to 17.61%, indicating that excessive NC content leads to structural defects, higher viscosity during mixing, and poor dispersion, which induce micro cracking and localized weaknesses susceptible to sulfate attack.

In mixes incorporating 10% TA, the strength loss pattern was less uniform. At 0% and 1% NC, losses were relatively moderate (8.09% and 8.98%, respectively), suggesting that low NC addition partially offsets the negative effect of TA's porosity. However, the loss dramatically rose to 19.19% at 3% NC and slightly decreased to 16.90% at 5% NC. This unexpected reversal indicates that while some NC improves gel continuity, higher NC combined with TA's elastic [98] and porous nature creates a heterogeneous matrix prone to cracking under expansive sulfate attack, accelerating deterioration [99].

For 25% TA mixes, a notable improvement occurred at 3% NC, where the strength loss dropped to 5.87%, the lowest among all mixtures tested. This suggests a synergistic effect between moderate NC addition and partial TA replacement, leading to an optimally compacted microstructure that resists ion ingress. However, at 5% NC, the loss rose to 11.07%, confirming that excessive NC still disrupts homogeneity, even when TA content is moderate.

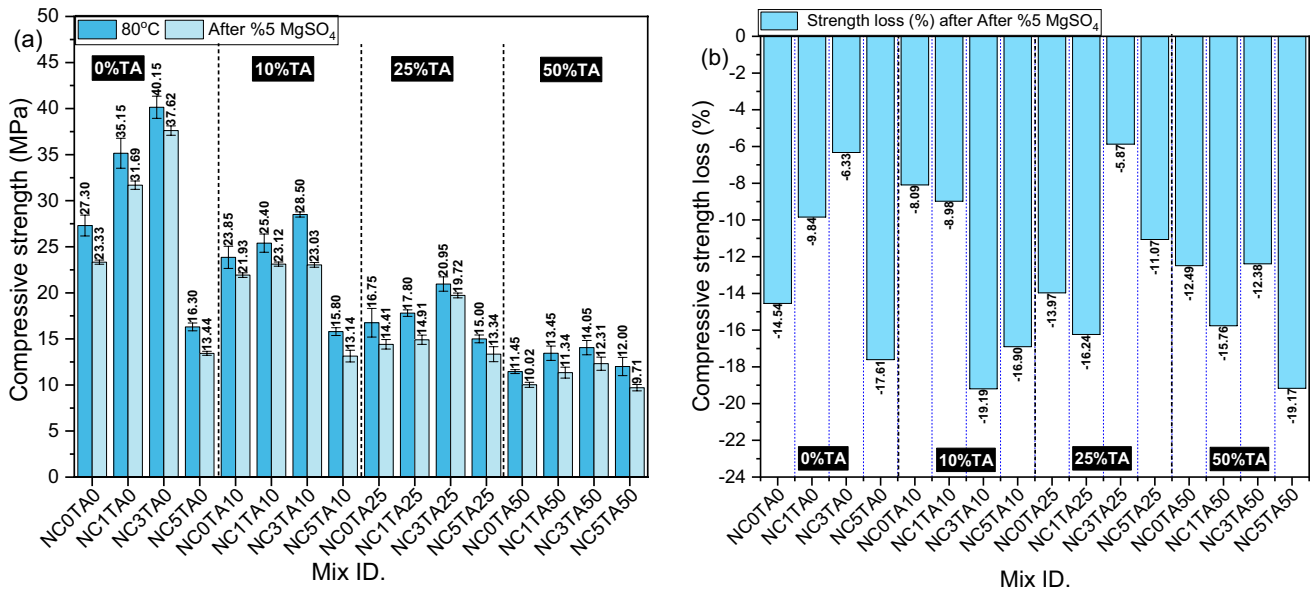


Fig. 16 Compressive strength values after heat curing at 80 °C (**a**) and strength loss (**b**) following sulfate attack

The 50% TA series showed the highest vulnerability, with losses ranging from 12.49% at 0% NC to 19.17% at 5% NC. High TA content significantly compromises durability due to its intrinsic porosity and weak bonding with the geopolymer matrix, creating pathways for Mg^{2+} ions to penetrate and trigger gypsum and brucite formation, leading to expansion [100] and cracking. Even the presence of NC could not counterbalance these detrimental effects at high TA levels [101].

Moderate NC levels (≈3%) substantially enhance sulfate resistance by refining the pore network and improving matrix density, reducing strength loss by up to 60% compared to the control. However, excessive NC (5%) reverses this benefit by inducing agglomeration and microstructural weaknesses.

Increasing TA content consistently increases susceptibility to sulfate attack due to its high porosity and poor interfacial bonding, which facilitate ion ingress and expansion-related cracking.

75% RS + 25% TA + 3% NC, exhibiting the lowest strength loss (5.87%), demonstrating optimal microstructural balance between densification and controlled flexibility.

90% RS + 10% TA + 3% NC (19.19% loss) and 50% RS + 50% TA + 5% NC (19.17% loss), where combined high TA and excessive NC caused severe microstructural disruption.

4.2 Weight loss

Figure 17a illustrates the weight loss of AACs after 120 days of immersion in a 5% $MgSO_4$ solution following thermal curing at 80 °C for 8 h. The results demonstrate that both NC incorporation and TA replacement significantly influence sulfate resistance through their effects on matrix densification, porosity, and interfacial quality.

For the control mixtures (0% TA), weight loss decreased from 2.42% at 0% NC to 2.10% at 1% NC and reached a minimum of 1.77% at 3% NC, indicating that moderate NC effectively densified the matrix and limited sulfate ingress. However, increasing the NC content to 5% increased weight loss to 3.81%, reflecting the adverse effects of particle agglomeration, reduced homogeneity, and micro-crack formation.

A similar trend was observed in the TA-containing mixtures. At 10% TA, weight loss remained relatively low at 0–1% NC, but increased to 2.63% at 3% NC and 3.79% at 5% NC. For the 25% TA series, the lowest weight loss (2.31%) was obtained with 3% NC, demonstrating that moderate NC partially compensated for the higher porosity introduced by TA. In contrast, the 50% TA mixtures exhibited the poorest sulfate resistance, with weight

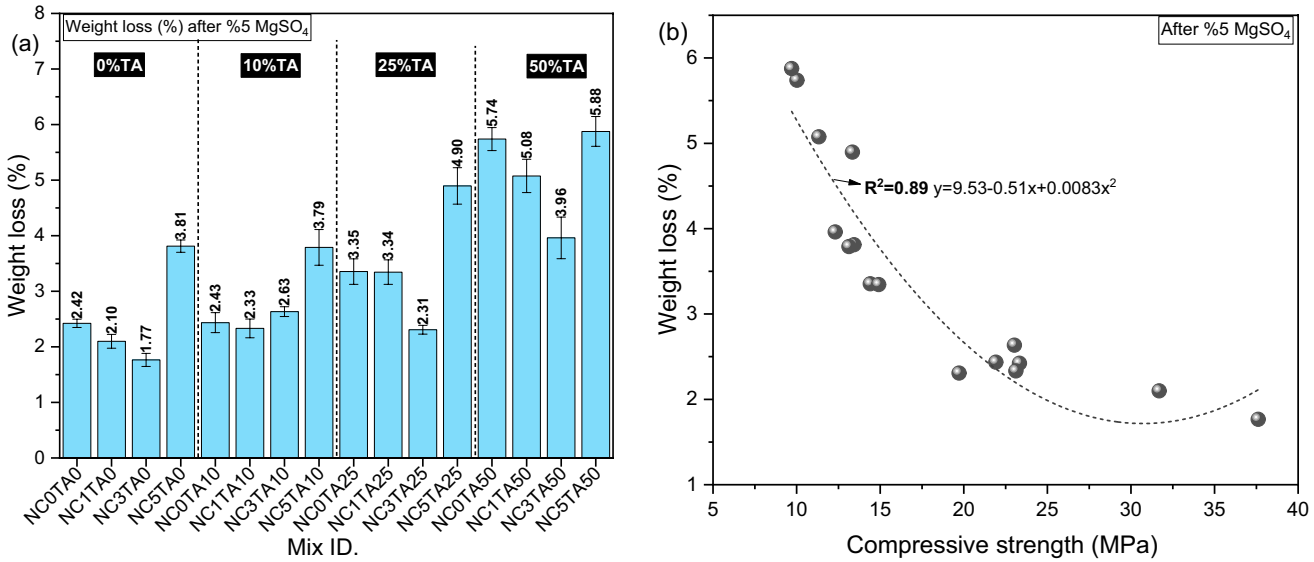


Fig. 17 **a** The weight loss following sulfate attack **b** compressive strength vs. weight loss

loss ranging from 5.74% to 5.88%, indicating that excessive TA dominated the deterioration process regardless of NC content.

moderate NC addition (≈3%) improved sulfate resistance by refining the pore structure and reducing ion penetration, whereas increasing TA content consistently increased weight loss because of higher porosity and weaker interfacial bonding. The best performance was obtained for the 0% TA-3% NC mixture (1.77%), whereas the 50% TA-5% NC mixture exhibited the highest weight loss (5.88%). Figure 17b further demonstrates a strong inverse correlation ($R^2 \approx 0.86$) between compressive strength and weight loss, indicating that sulfate-induced matrix degradation, associated with gypsum/brucite formation and gel deterioration, directly reduced the residual mechanical performance.

4.3 Microstructural analysis

4.3.1 SEM observations

Figure 18a presents the SEM microstructure of the NC5TA0 mixture (95% GBFS, 5% NC, 100% RS, 0% TA) after curing at 80 °C for 8 h and immersion in 5% $MgSO_4$ solution for 120 days. This mixture exhibited a compressive strength loss of 17.61%, indicating limited sulfate resistance at excessive NC content. The microstructure is characterized by extensive micro-cracking, voids, binder disruption, and numerous spherical pits associated with sulfate attack. Localized deposits, attributed to ettringite and gypsum, are observed within cracks and pores. Excessive NC promoted particle agglomeration and matrix heterogeneity, creating weak zones that facilitated sulfate ingress and accelerated deterioration. These features explain the relatively high strength loss of the mixture.

Figure 18b shows the SEM microstructure of the NC0TA10 mixture (100% GBFS, 10% TA) after the same sulfate exposure. This mixture exhibited a compressive strength loss of only 8.09%. Compared with NC5TA0, the matrix remained denser and more coherent, with fewer and narrower micro-cracks and only limited sulfate-related deposits. The incorporation of 10% TA appears to have provided localized strain accommodation, reducing crack propagation and preserving matrix continuity, thereby improving sulfate resistance.

Figure 18c illustrates the SEM microstructure of the NC3TA0 mixture after sulfate exposure. The matrix remains relatively dense and continuous, consistent with its low compressive strength loss (6.33%). Narrow, discontinuous micro-cracks and the absence of extensive voids indicate that 3% NC effectively refined the pore structure, reduced pore connectivity, and restricted sulfate ingress. Only minor localized deposits were observed, suggesting limited sulfate-induced deterioration.

Figure 18d presents the SEM microstructure of the optimal NC3TA25 mixture, which exhibited the lowest compressive strength loss (5.87%). Despite the incorporation of 25% TA, the matrix remained compact, with dense gel regions and only localized interfacial gaps around TA particles. Crack propagation was limited, indicating that nano-clay-induced pore refinement and the stress-accommodating effect of TA acted synergistically to maintain matrix integrity and improve sulfate resistance.

Figure 18e shows the SEM microstructure of the NC5TA50 mixture after sulfate exposure. This mixture exhibited the highest compressive strength loss (19.17%), accompanied by severe microstructural deterioration. Extensive interconnected cracks, large voids, weak interfacial transition zones, and fragmented reaction products indicate substantial matrix degradation. The combined effects of excessive NC agglomeration and high TA content increased porosity, weakened gel continuity, and facilitated sulfate ingress, resulting in the poorest durability among all mixtures.

4.3.2 EDS results

Figure 19a presents the SEM–EDS analyses of the NC5TA0 mixture (95% GBFS, 5% NC, 100% RS, 0% TA) after curing at 80 °C for 8 h and immersion in 5% $MgSO_4$ solution for 120 days. This mixture exhibited a

 https://doi.org/10.1007/s43452-026-01614-2

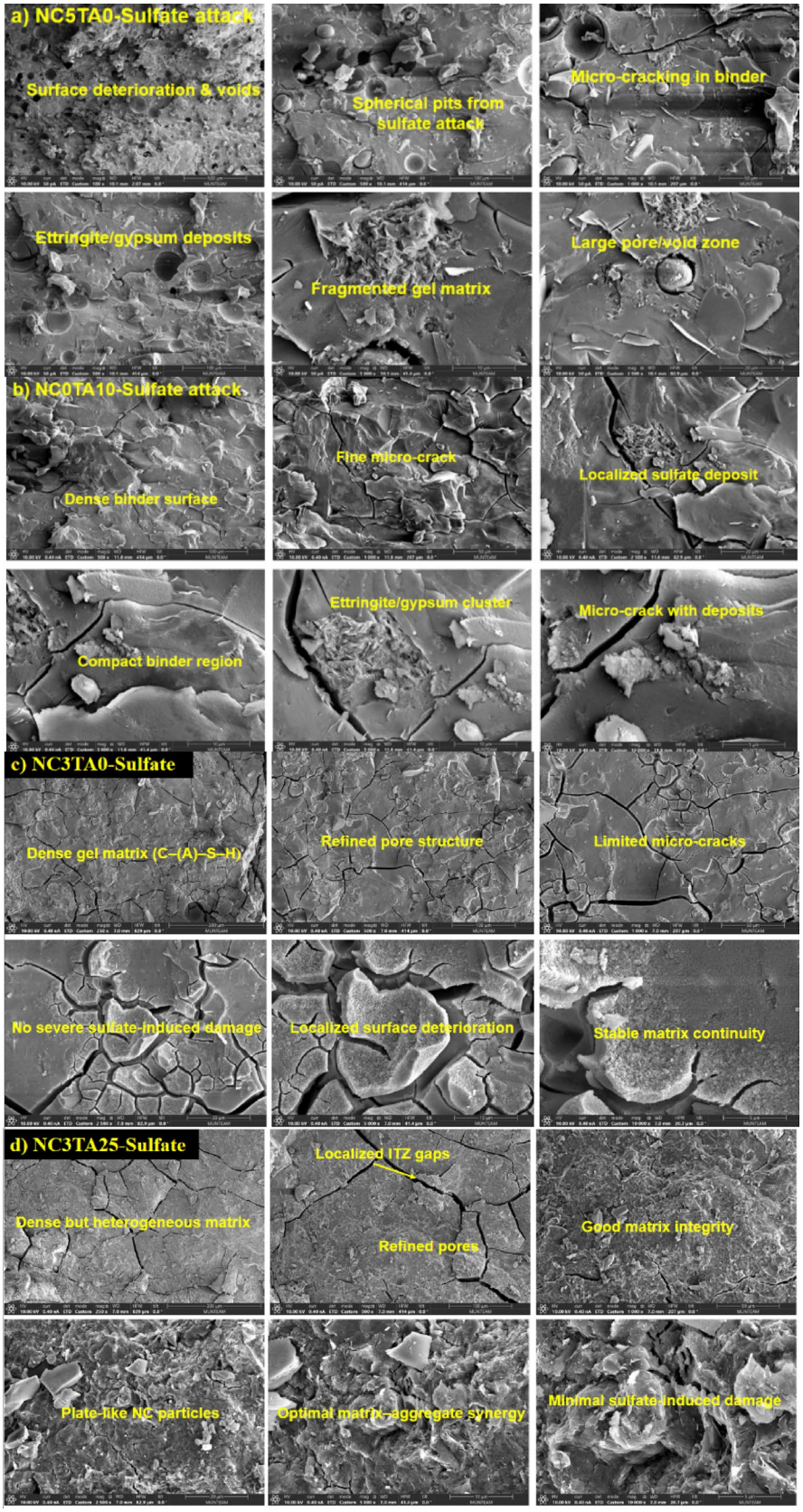


Fig. 18 Microstructural characteristics after sulfate attack **a** NC5TA0 **b** NC0TA10 **c** NC3TA0 **d** NC3TA25 **e** NC5TA50

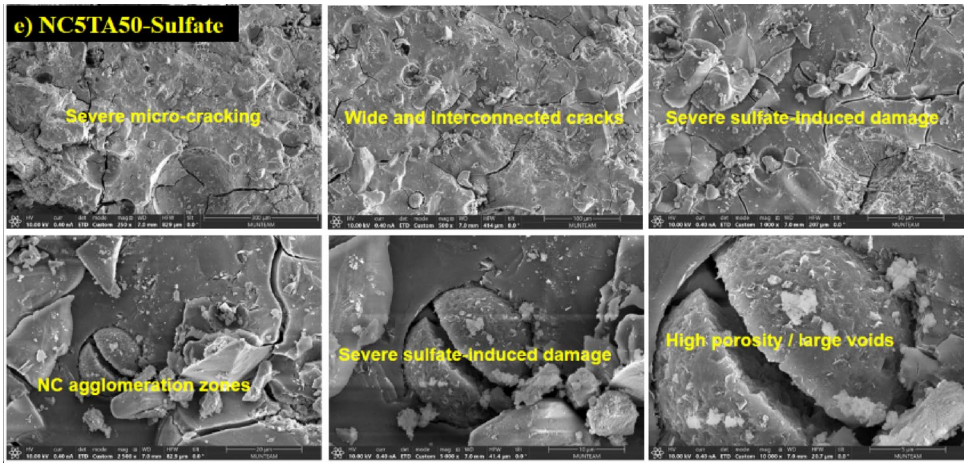


Fig. 18 (continued)

compressive strength loss of 17.61%, indicating limited sulfate resistance at excessive NC content. SEM observations reveal a porous and fragmented matrix with numerous spherical pits, voids, micro-cracks, and localized deposits attributed to ettringite and gypsum. These features indicate that excessive NC promoted agglomeration and matrix heterogeneity, facilitating sulfate ingress. EDS analysis, dominated by O (46.6 wt%), Si (17.0 wt%), Ca (15.4 wt%), Na (6.4 wt%), and Al (3.8 wt%), confirms degradation of the C-(A)-S-H gel, while Mg (2.1 wt%) reflects sulfate-related reaction products. These observations explain the relatively high strength loss.

Figure 19b presents the SEM-EDS analyses of the NC0TA10 mixture after the same sulfate exposure. This mixture exhibited a compressive strength loss of only 8.09%. The SEM image shows a relatively dense matrix with limited and discontinuous micro-cracks, indicating reduced sulfate-induced damage. Localized sulfate deposits are present but do not significantly disrupt matrix continuity. The incorporation of 10% TA appears to have provided strain-accommodating zones that reduced crack propagation. EDS results, characterized by O (47.0 wt%), Si (17.4 wt%), Ca (14.5 wt%), Na (5.9 wt%), and Al (4.8 wt%), confirm the persistence of C-(A)-S-H gels, while Mg (2.6 wt%) indicates only limited sulfate reaction products. The comparatively compact microstructure explains the improved sulfate resistance.

Figure 19c presents the SEM–EDS analyses of the NC3TA0 mixture after sulfate exposure. The matrix remains dense and continuous with only localized micro-cracks, consistent with its low compressive strength loss (6.33%). EDS analysis confirms that the matrix is dominated by O, Ca, and Si, indicating well-developed C-(A)-S-H gels with hybrid alkali-aluminosilicate phases. The limited presence of sulfate reaction products suggests that 3% NC effectively refined the pore structure and restricted sulfate ingress, thereby preserving matrix integrity.

Figure 19d presents the SEM-EDS analyses of the NC3TA25 mixture, which exhibited the lowest compressive strength loss (5.87%). Although localized interfacial gaps are observed around the TA particles, the matrix remains compact and crack propagation is limited. EDS results confirm the persistence of C-(A)-S-H gels together with hybrid gel phases, while only minor sulfate-related products are detected. The combined effects of nano-clay-induced pore refinement and the stress-accommodating behavior of 25% TA produced the most stable microstructure and the highest sulfate resistance.

Figure 19e presents the SEM-EDS analyses of the NC5TA50 mixture after sulfate exposure. This mixture exhibited the highest compressive strength loss (19.17%). SEM observations reveal severe microstructural deterioration characterized by interconnected cracks, fragmented gel regions, weak ITZs, and large discontinuities. The combined effects of excessive NC agglomeration and high TA content increased porosity and weakened matrix continuity, accelerating sulfate ingress. EDS analysis indicates residual C-(A)-S-H gels together with limited hybrid gel formation, suggesting that deterioration was mainly governed by decalcification and structural

 https://doi.org/10.1007/s43452-026-01614-2

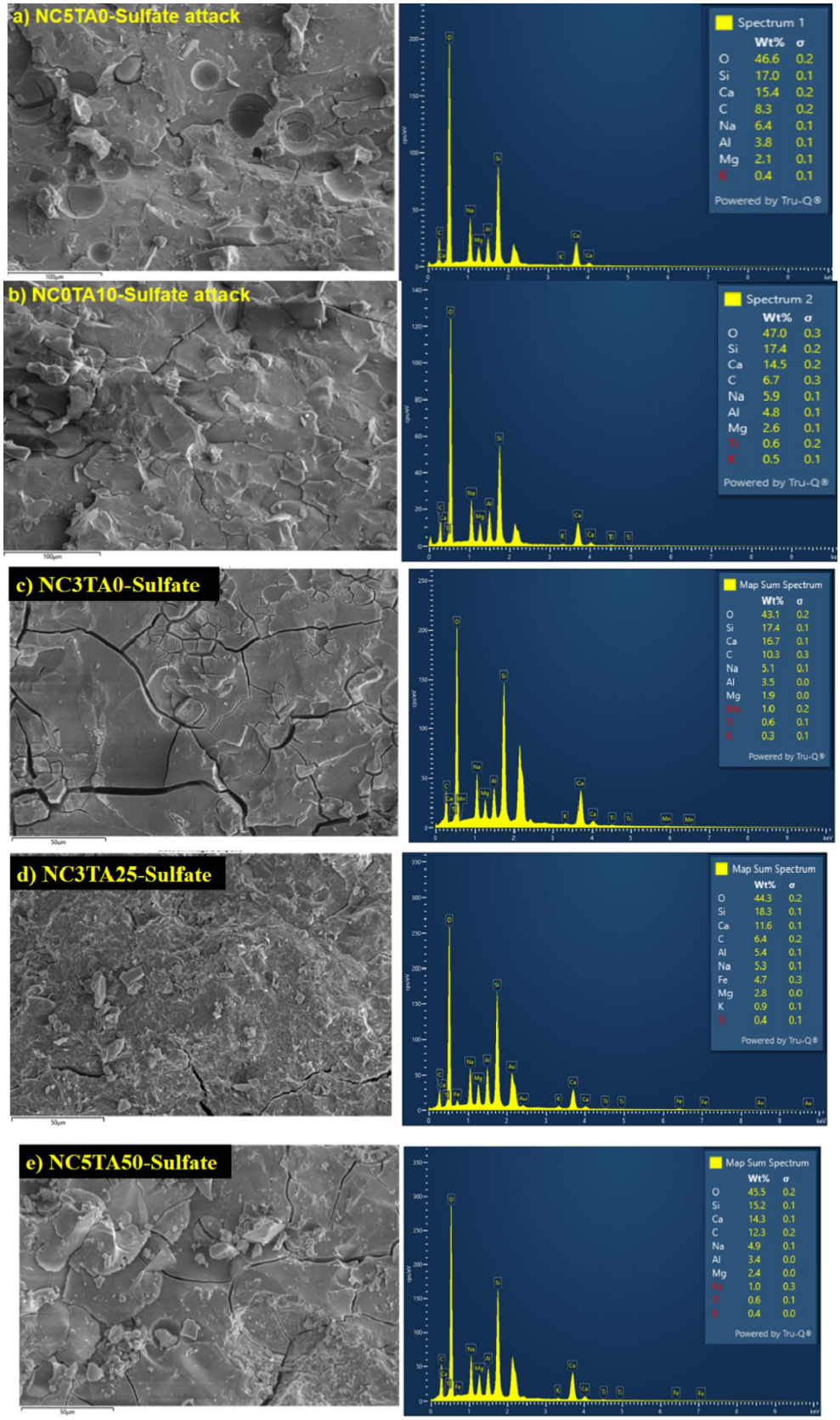


Fig. 19 EDS results after sulfate attack **a** NC5TA0 **b** NC0TA10 **c** NC3TA0 **d** NC3TA25 **e** NC5TA50

disintegration rather than extensive secondary phase formation. These features explain the poorest durability performance among all mixtures.

Figure 20 presents the XRD patterns of NC3TA0, NC3TA25, and NC5TA50 mixtures after sulfate exposure. All mixtures exhibit a broad amorphous hump in the range of approximately 20–35° (2θ), confirming that the matrix is predominantly composed of amorphous C-(A)-S-H type gels. However, notable differences in peak intensity and crystallinity are observed among the mixtures.

The NC3TA0 mixture shows a relatively smooth amorphous profile with limited crystalline peaks, indicating a stable and well-developed gel structure with minimal formation of secondary crystalline phases. In contrast, the NC3TA25 mixture exhibits slightly increased peak intensity, suggesting limited formation of sulfate-related products; however, the overall amorphous character is still preserved, consistent with its superior durability performance.

The NC5TA50 mixture displays more pronounced and sharper peaks, indicating increased crystallinity and the formation of degradation-related phases. This behavior can be attributed to higher sulfate interaction, partial gel decomposition, and structural instability. The reduction in amorphous hump intensity further suggests disruption of the gel network.

The XRD results confirm that mixtures with moderate NC content maintain a more stable amorphous gel structure, while excessive NC and high TA content promote crystallization and degradation, correlating well with the observed strength losses and SEM findings.

Figure 21 presents the FTIR spectra of NC3TA0, NC3TA25, and NC5TA50 mixtures after sulfate exposure, highlighting changes in the chemical structure of the binder. All mixtures exhibit a broad band around ~950–1000 cm^{-1}, corresponding to Si–O–T (T = Si or Al) asymmetric stretching, which is characteristic of C-(A)-S-H / N-A-S-H type gel structures.

The NC3TA0 mixture shows a relatively sharp and well-defined band in this region, indicating a more polymerized and stable gel network. In the NC3TA25 mixture, this band is slightly broadened and shifted, suggesting minor structural reorganization of the gel due to limited sulfate interaction; however, the overall integrity of the aluminosilicate network is largely preserved.

In contrast, the NC5TA50 mixture exhibits a noticeable broadening and reduced intensity of the main Si-O-T band, indicating partial depolymerization and weakening of the gel structure. Additionally, more pronounced bands in the ~1400–1500 cm^{-1} region can be associated with carbonate or sulfate-related products, reflecting increased chemical interaction and degradation. The band near ~3400 cm^{-1} (O-H stretching) is also more intense in this mixture, suggesting higher bound water content and increased porosity.

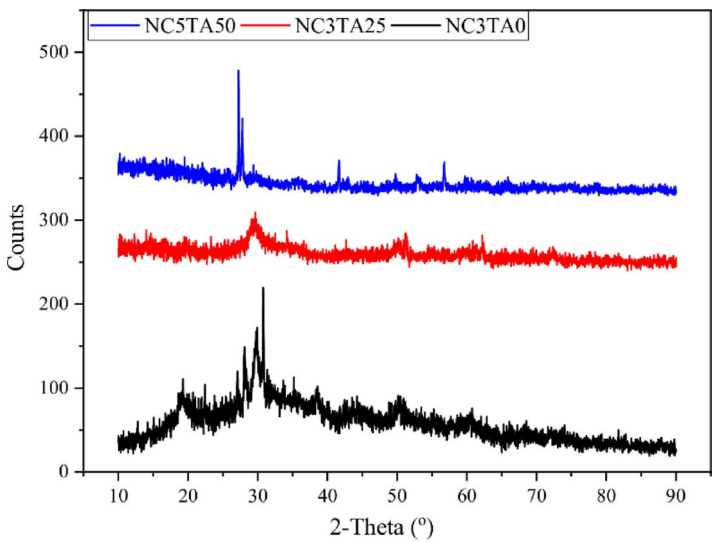


Fig. 20 XRD results after sulfate attack of the mixtures; NC3TA0, NC3TA25 and NC5TA50

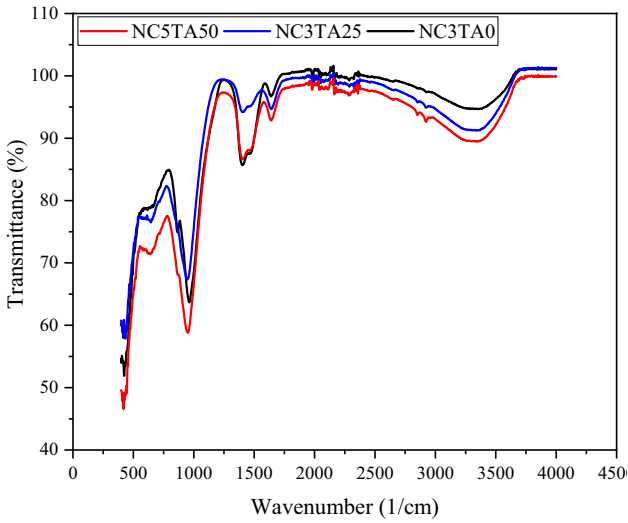


Fig. 21 FTIR results after sulfate attack of the mixtures; NC3TA0, NC3TA25 and NC5TA50

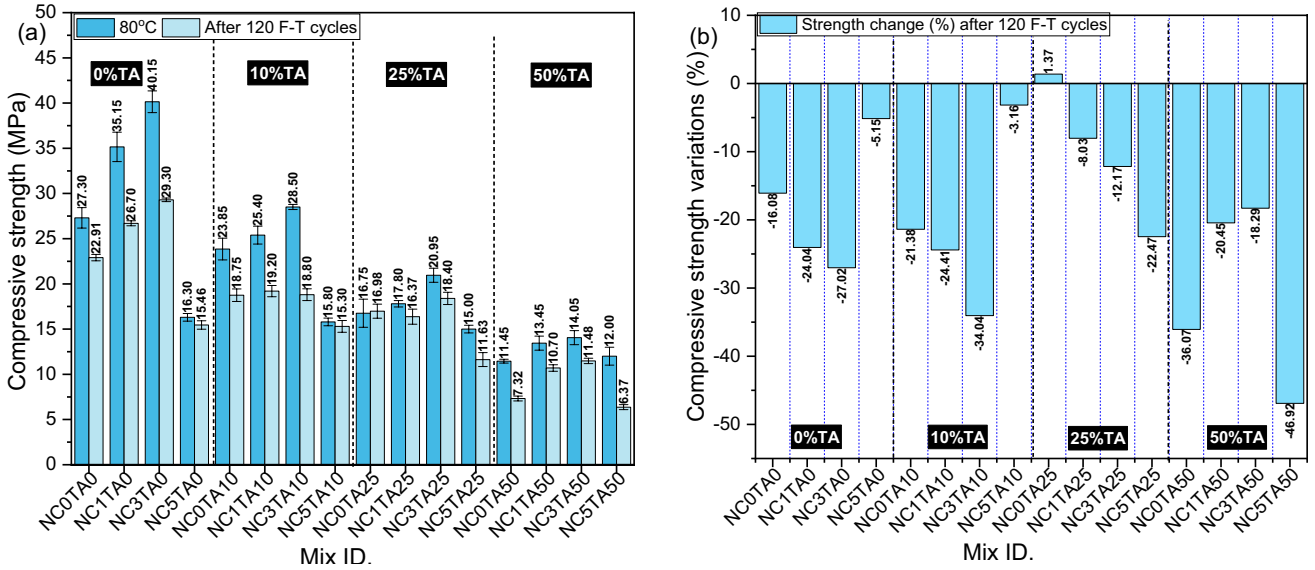


Fig. 22 Compressive strength values cured at 80 °C and after exposure to 120 F–T cycles (**a**) and strength loss (**b**) following 120 F-T cycles

The FTIR results confirm that mixtures with moderate NC content maintain a more stable and polymerized gel structure, whereas excessive NC and high TA content lead to gel depolymerization, increased secondary reaction products, and reduced chemical stability-consistent with the observed mechanical and durability performance.

5 Exposure to 120 freeze-thaw cycles

5.1 The compressive strength

Figure 22a and b illustrate the freeze–thaw (F-T) durability of slag-based AACs, highlighting the effects of NC addition and TA replacement on compressive strength retention after 120 cycles. The results reveal that the resistance to cyclic frost damage is governed by a complex interplay between matrix densification, pore connectivity, and ITZ performance, which are strongly influenced by NC dosage and TA incorporation.

For the reference mixture with 100% RS and no TA, compressive strength loss followed a non-linear pattern: 16.03% at 0% NC, increasing to 24.04% and 27.02% at 1% and 3% NC, but then decreasing sharply to 5.15% at 5% NC. While low to moderate NC dosages likely intensified brittleness and stress concentration, the unexpected improvement at 5% may be attributed to a combined filler and nucleation effect, which refined the pore structure and improved matrix homogeneity [34]. Although higher NC contents are often associated with agglomeration and increased porosity in the literature [102], in this case the refined microstructure appears to have counteracted these drawbacks, limiting water ingress and internal pressure under F-T cycles [103].

The incorporation of 10% TA altered the freeze–thaw response of the mixtures, leading to a non-linear trend with respect to NC content. At 0% and 1% NC, compressive strength losses were 21.38% and 24.41%, respectively, indicating that the elastic and porous nature of TA introduced micro-voids and weak ITZs, which facilitated water ingress and accelerated damage under cyclic freezing conditions.

At 3% NC, the strength loss increased to 34.04%, representing the highest value in this series. Although this NC level provides optimum matrix densification under normal conditions, the resulting dense and relatively stiff structure may reduce the ability of the system to accommodate internal stresses generated during F-T cycles [104]. In the presence of weak TA-paste interfaces, this stiffness can intensify stress concentration and promote micro crack propagation, leading to increased deterioration.

In contrast, at 5% NC, the strength loss decreased significantly to 3.16%, the lowest among all tested mixtures. This behavior can be attributed to the combined effects of partial NC agglomeration and increased microstructural heterogeneity, which may slightly increase porosity and reduce stiffness, thereby enhancing stress accommodation during cyclic freezing and thawing. When combined with the deformable nature of TA, this results in reduced internal stress concentration and improved resistance to F-T damage. These results indicate that F-T performance is governed by a balance between matrix densification and stress accommodation capacity, rather than by densification alone [105].

In the 25% TA series, an unusual phenomenon was observed: a slight strength gain of 1.37% at 0% NC, likely due to the flexible nature of TA absorbing and redistributing stress during freezing, resulting in improved structural integrity [103]. However, this benefit diminished with NC incorporation, as losses reached 12.17% and 22.47% at 3% and 5% NC, respectively. The combination of higher NC content and moderate TA replacement may have increased matrix stiffness and reduced deformability, leading to micro crack propagation under repeated volumetric changes. Furthermore, agglomeration of excess NC could introduce flaws, acting as stress initiators under cyclic thermal gradients.

The most pronounced deterioration occurred in the 50% TA series, where compressive strength losses ranged from 36.07% at 0% NC to 46.92% at 5% NC, despite a brief improvement at 3% NC (18.29%). These findings confirm that excessive TA incorporation severely compromises F-T resistance [106], primarily due to its high porosity, low bonding strength with the binder, and susceptibility to ITZ degradation [107]. These factors create interconnected void networks, increasing water absorption and allowing frost-induced expansion, leading to matrix disintegration. Even high NC dosages could not counteract these detrimental effects, as the combination of TA-induced heterogeneity and NC-induced stiffening promoted crack formation and propagation.

The results underscore that F-T durability of AACs depends on achieving an optimal balance between densification and flexibility. NC addition up to 5% significantly enhances performance when TA content is low ($\leq$10%), reducing compressive strength loss by more than 80% compared to the control. However, in systems with high TA content ($\geq$50%), the negative influence of weak ITZ and excessive porosity dominates, rendering NC addition ineffective. The best-performing mixture was 90% RS + 10% TA + 5% NC, exhibiting only 3.16% strength loss, while the poorest performance was recorded in the 50% TA + 5% NC mixture, with nearly 47% loss. These findings highlight the necessity for tailored mix designs that combine NC's microstructural refinement benefits with controlled TA incorporation to achieve frost-resistant sustainable composites.

 https://doi.org/10.1007/s43452-026-01614-2

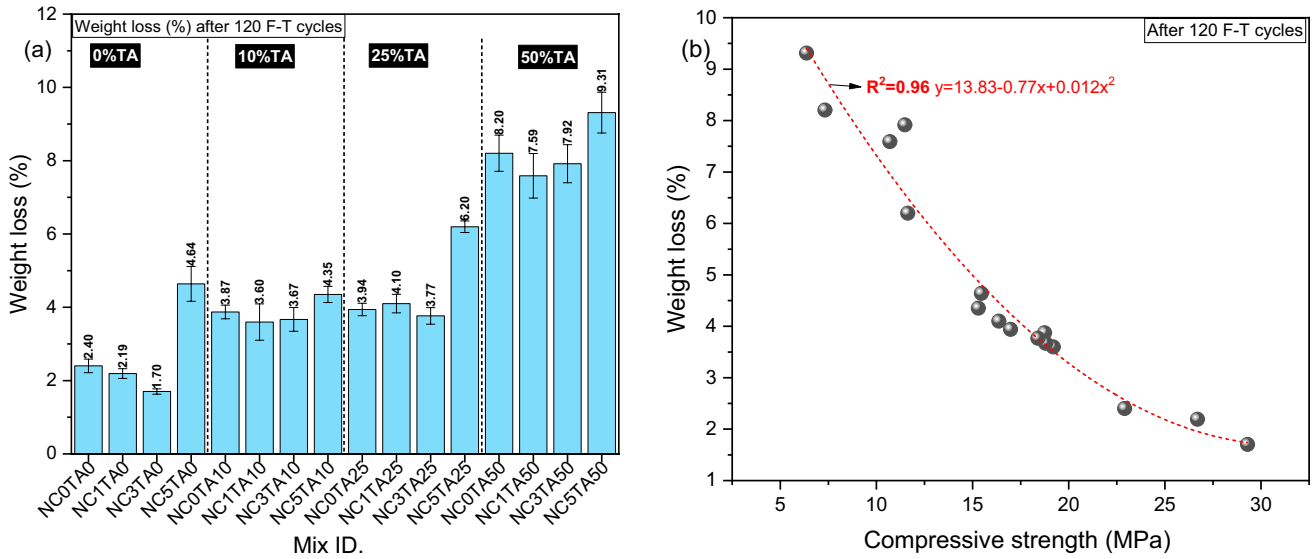


Fig. 23 **a** Weight loss on exposure to 120 F-T cycles **b** compressive strength vs. weight loss

5.2 Weight loss

Figure 23a illustrates the weight loss behavior of AACs after 120 F-T cycles, providing insights into the combined effects of NC incorporation and TA replacement on frost durability. The control mix with 100% RS demonstrated progressive improvement with increasing NC content up to 3%, where weight loss decreased from 2.40% at 0% NC to 2.19% at 1% NC and reached a minimum of 1.70% at 3% NC. This significant reduction indicates that moderate NC dosage contributes to pore refinement and densification through its filler effect and surface reactivity, which enhance the continuity of geopolymer gels and reduce permeability [108], thereby mitigating internal stress buildup during freezing and thawing cycles [109]. However, at 5% NC, weight loss sharply increased to 4.64%, likely due to agglomeration, poor dispersion, and increased water demand associated with excessive NC, which introduces microstructural heterogeneity and localized weaknesses prone to cracking under cyclic stress.

For mixes with partial TA replacement, frost resistance declined markedly compared to RS-based mixtures, primarily due to TA's high porosity and weak interfacial bonding, which facilitate water ingress and create stress concentration zones during freeze–thaw cycles. At 10% TA, weight loss ranged from 3.87% to 4.35%, slightly improving at 1% NC but deteriorating with higher NC levels. Similarly, at 25% TA, losses were between 3.94% and 6.20%, reflecting the inability of NC beyond 1–3% to counteract the detrimental effects of TA's elastic and porous nature. The 50% TA series exhibited the poorest performance, with weight loss values of 8.20%, 7.59%, 7.92%, and 9.31% at 0%, 1%, 3%, and 5% NC, respectively, confirming that high TA content severely compromises durability by introducing interconnected voids that accelerate scaling and surface deterioration under frost exposure.

The best F-T resistance was achieved by the mix containing 100% RS and 3% NC (1.70% weight loss), demonstrating that moderate NC addition effectively improves microstructural stability and water resistance. In contrast, the worst performance occurred with 50% TA and 5% NC (9.31% weight loss), where excessive TA and NC combined to produce a highly porous [110] and heterogeneous matrix vulnerable to frost-induced damage [111]. These findings highlight the critical need to optimize NC dosage and limit TA content to balance sustainability goals with long-term durability under severe cyclic freezing conditions. Figure 23b depicts the correlation between compressive strength and weight loss of AACs after 120 F–T cycles, highlighting the inverse relationship between these parameters. The plotted trend demonstrates a strong negative quadratic correlation ($R^2 = 0.96$), indicating that as weight loss increases, compressive strength decreases significantly, with the rate

of strength reduction accelerating beyond a certain threshold of material degradation. Mixtures with low weight loss (≤ 2%)-primarily those incorporating 100% RS and moderate NC (1–3%)-retained superior compressive strength, confirming the critical role of reduced porosity and refined microstructure in enhancing frost durability. Conversely, mixes with higher weight loss (≥ 6%), particularly those containing 50% TA, exhibited drastic compressive strength reductions, reflecting severe matrix damage and surface scaling under cyclic freezing conditions.

6 Sustainability and CO_2 balance assessment

This study demonstrates the dual sustainability benefits of NC addition and TA substitution in AACs. By partially replacing natural sand with TA, the environmental burden of tire disposal is reduced while simultaneously preserving finite natural resources. Sand mining is increasingly linked to river ecosystem degradation and biodiversity loss [112], and diverting end-of-life tires from landfills mitigates risks of uncontrolled burning and micro plastic pollution [113]. Recycling waste tires into AACs thus provides both environmental and resource conservation benefits.

Similarly, incorporating small dosages of NC (≤ 3%) improves matrix densification without requiring energy-intensive synthesis, unlike nano-silica or nano-alumina. NC, derived from abundant montmorillonite or smectite clays [114], is recognized as a low-cost, widely available, and eco-friendly additive [115]. Previous research has shown that NC addition reduces permeability and enhances durability while requiring substantially less energy compared to synthetic nanoparticles [116]. This makes NC a greener alternative in high-performance binder systems.

The CO_2 balance indicates that the proposed AAC system significantly lowers embodied carbon compared with ordinary Portland cement (OPC)-based concrete. OPC production is known to release ~ 0.9 ton CO_2 per ton of clinker, accounting for ~ 7–8% of global anthropogenic emissions [2]. In contrast, GBFS-based AACs avoid calcination-related emissions since slag is an industrial by-product with allocated carbon burdens already attributed to steel production [117]. Life cycle assessments (LCA) have shown that AACs can reduce embodied carbon by 40–80% depending on mix design and curing regime. At the optimized mix design (3%NC-25%TA), this study achieved durable performance with an estimated 40–55% reduction in CO_2 footprint relative to OPC concretes, consistent with earlier findings by Yang et al. [118].

Beyond CO_2 savings, the use of waste tire aggregates supports circular economy principles by transforming a non-biodegradable waste stream into a value-added construction resource. This approach directly contributes to the United Nations Sustainable Development Goals (SDGs), particularly SDG 9 (Industry, Innovation, and Infrastructure), SDG 11 (Sustainable Cities and Communities), SDG 12 (Responsible Consumption and Production), and SDG 13 (Climate Action) [119]. Moreover, the NC–TA hybrid system helps prevent rebound effects-where maximum strength is achieved at the expense of sustainability—by offering a balance between mechanical, durability, and environmental performance [120].

The findings confirm that NC- and TA-modified AACs offer a practical route to decarbonizing the construction sector. By lowering embodied emissions, valorizing industrial by-products, and minimizing the extraction of virgin raw materials, this system supports the transition toward net-zero carbon infrastructure and eco-efficient building practices.

7 Conclusion

This study comprehensively evaluated the influence of nano-clay (NC) and waste tire aggregate (TA) on the mechanical, physical, and durability properties of GBFS-based alkali-activated composites (AACs). The findings, expressed through both quantitative and qualitative analyses, indicate that the overall performance of AACs

is governed by the coupled interaction between nano-scale matrix densification induced by NC and macro-scale interfacial behavior introduced by TA, rather than by their individual contributions alone. The key results are summarized as follows:

(a) Incorporation of NC (up to 5%) resulted in notable strength enhancement, with compressive strength increasing by approximately 10–18% and flexural strength by 8–15%, primarily due to improved matrix densification and accelerated geopolymeric reactions, with the optimum performance observed at approximately 3% NC.
(b) Partial replacement of natural river sand with TA (up to 25%) preserved compressive strength at approximately 90–95% of the control while reducing bulk density by 5–12%, indicating that TA levels up to 25% provide an optimal balance between mechanical performance and lightweight characteristics.
(c) NC addition refined the pore structure and reduced water absorption by 6–10%, whereas TA increased open porosity but contributed to a reduction in overall unit weight; the lowest porosity and absorption values were obtained at approximately 3% NC with low-to-moderate TA content.
(d) Sorptivity values decreased in NC-modified mixtures, with the minimum values recorded at 3% NC, confirming the effectiveness of this dosage in enhancing microstructural compactness.
(e) Under sulfate exposure, mixtures containing approximately 3% NC and ≤25% TA exhibited the lowest compressive strength loss (≤12%) and mass loss (<5%), indicating optimum chemical durability.
(f) Freeze–thaw results indicated that combined NC–TA incorporation improved residual strength retention by approximately 8–14%, with the most stable performance observed in mixtures containing moderate NC (approximately 3%) and limited TA (≤25%).
(g) High-temperature performance showed that NC-modified mixtures retained up to 70–75% of their original strength at 400 °C, with 3% NC mixtures demonstrating the highest thermal stability, while TA contributed to mitigating explosive spalling.
(h) SEM observations revealed that NC promoted the formation of dense and continuous gel phases, particularly at optimum NC levels (around 3%), resulting in improved matrix integrity and enhanced ITZ quality.
(i) The plate-like morphology of NC particles provided effective nucleation sites, with the most homogeneous gel distribution achieved at moderate NC contents, beyond which agglomeration occurred.
(j) TA particles, due to their porous and deformable nature, contributed to stress redistribution and crack resistance; however, this effect remained beneficial only at moderate replacement levels (≤25%).
(k) The utilization of TA offers a sustainable pathway for recycling end-of-life tires while reducing dependence on natural aggregates, particularly at optimum replacement levels.
(l) The use of NC within GBFS-based systems contributes to lowering the carbon footprint, especially when combined with optimized NC–TA proportions.
(m) The combined use of NC and TA demonstrates a balanced performance: NC enhances strength and durability through matrix densification, whereas TA reduces density and improves energy absorption, with the best performance achieved at approximately 3% NC and ≤25% TA.
(n) The results confirm that AAC performance is governed by the coupled interaction between nano-scale densification and macro-scale interfacial behavior, with optimum properties obtained when these effects are balanced at approximately 3% NC and ≤25% TA, resulting in composites that are both structurally efficient and environmentally sustainable.

7.1 Research limitations

(a) The investigation was limited to specific NC dosages (0–5%) and TA substitution levels (0–50%), and broader compositional ranges were not explored.

(b) Only one thermal curing regime (80 °C for 8 h) was applied; the influence of alternative curing conditions (e.g., ambient or multi-stage curing) was not evaluated.
(c) Durability assessment focused on sulfate exposure, freeze–thaw cycles, and high-temperature resistance. Other aggressive environments, such as chloride ingress and carbonation, were not included within the scope of this study.
(d) Microstructural and phase analyses (SEM–EDS, XRD, and FTIR) were primarily conducted on sulfate-exposed samples to evaluate degradation mechanisms under the most critical exposure condition. While this approach enables a focused and mechanism-oriented interpretation, further characterization of unexposed and differently conditioned samples could provide additional insight.

7.2 Recommendations for future research

(a) Extend the range of NC and TA dosages and evaluate their performance under different curing regimes, including ambient, steam, and hybrid curing conditions.
(b) Investigate durability under additional environmental exposures such as chloride penetration, carbonation, and combined chemical–mechanical actions to better simulate real service conditions.
(c) Perform comprehensive multi-technique characterization (e.g., TG/DTG, BET, MIP, and micro-CT) on both unexposed and exposed samples to further quantify pore structure evolution, gel chemistry, and degradation mechanisms.
(d) Examine the behavior of scaled-up elements and structural components to validate laboratory findings and assess field applicability.
(e) Conduct detailed life-cycle assessment (LCA) and cost–performance analyses to strengthen the sustainability and practical implementation potential of these materials.

One strategy that has gained increasing attention is the incorporation of nanomaterials into alkali-activated systems [23–25]. Nanoparticles, owing to their extremely high surface area and reactivity, can serve as nucleation sites, accelerate.

Funding This research received no external funding.

Data availability The data that support the findings of this study are available from the corresponding author upon reasonable request.

Declarations

Conflict of interest The author declares that he has no conflict of interest.

Ethical approval This article does not contain any studies with human participants or animals performed by any of the authors.

References

1. Andrew RM. Global CO 2 emissions from cement production. Earth Syst Sci Data. 2018;10(1):195–217.
2. Environment U, Scrivener KL, John VM, Gartner EM. Eco-efficient cements: Potential economically viable solutions for a low-CO2 cement-based materials industry. Cem Concr Res. 2018;114:2–26.
3. Yilmazoglu MU, Türkel I, Benli A, Bayraktar OY, Bilgehan M, Kaplan G. Sustainable enhancement of alkali-activated foam concrete using vegetable waste ash and fly ash: Improving mechanical, thermal, and durability properties. J Building Eng. 2025;110:113091.

4. Yılmazoğlu MU, Kara HO, Benli A, Demirkıran AR, Bayraktar OY, Kaplan G. Sustainable alkali-activated foam concrete with pumice aggregate: effects of clinoptilolite zeolite and fly ash on strength, durability, and thermal performance. Constr Build Mater. 2025;464:140160.
5. Dieuhou CM, Ngnie G, Tchekwagep JJK, Mbole BRE, Tchakouté HK, Li ZH, Rüscher CH, Nanseu-Njiki CP, Hou PK. Influence of adding silica sand powder on the macroscopic properties and microscopic pore structures of waste-fired clay brick-based geopolymers. Arch Civ Mech Eng. 2025;25(4).
6. Miller SA, Horvath A, Monteiro PJ. Impacts of booming concrete production on water resources worldwide. Nat Sustain. 2018;1(1):69–76.
7. Chen WW, Shen PL, Qin QL, Tao Y, Poon CS. Synthesis of low-carbon alkali-activated materials using carbonated recycled concrete fines with sodium meta-aluminate. Cem Concrete Comp. 2025;163.
8. Öz A, Yilmaz MK, Benli A, Kaplan G. Sustainable prepacked alkali-activated concrete: influence of natural zeolite, recycled aggregate, and curing conditions on mechanical, durability, and thermal performance. Arch Civ Mech Eng. 2025;25(5–6).
9. Öz A, Dursun FM, Benli A, Kaplan G. Optimization of sustainable high-performance alkali-activated composites using industrial and agricultural wastes: A comprehensive performance evaluation. J Building Eng. 2025;111.
10. Bayrak B, Benli A, Alcan HG, Çelebi O, Kaplan G, Aydin AC. Recycling of waste marble powder and waste colemanite in ternary-blended green geopolymer composites: Mechanical, durability and microstructural properties. J Building Eng. 2023;73:106661.
11. Bayrak B, Öz A, Benli A, Kavaz E, Kaplan G, Aydın AC. Physico-mechanical and shielding properties of alkali-activated slag composites incorporating cement clinker aggregate: Effect of high temperature and particle size. J Building Eng. 2023;67:105982.
12. Sevim O, Alakara EH, Demir I, Bayer IR. Effect of magnetic water on properties of slag-based geopolymer composites incorporating ceramic tile waste from construction and demolition waste. Arch Civ Mech Eng. 2023;23(2):107.
13. Bayrak B, Ipek S, Alcan HG, Kaplan G, Aydin AC, Güneyisi E. Engineering and microstructural properties of environmentally friendly alkali-activated composites containing clinker aggregate: heat-curing regime and elevated-temperature effect. Arch Civ Mech Eng. 2024;24(4):200.
14. Elahi MMA, Hossain MM, Karim MR, Zain MFM, Shearer C. A review on alkali-activated binders: Materials composition and fresh properties of concrete. Constr Build Mater. 2020;260:119788.
15. Rakhimova N, Shi CJ. Upcycling of concrete wastes as precursors in alkali-activated materials: a review. Constr Build Mater. 2024;436:136978.
16. Yaswanth KK, Reddy KHK, Anusha N, Praveen B, Chippymol J, Revathy J, Isleem HF. Engineered geopolymer composites: a comprehensive state-of-the-art review on materials' perspective. Arch Civ Mech Eng. 2024;24(3).
17. Xue CH, Sirivivatnanon V, Nezhad A, Zhao QX. Comparisons of alkali-activated binder concrete (ABC) with OPC concrete-a review. Cem Concrete Comp. 2023;135:104851.
18. Kong Y, Kurumisawa K. Fresh properties and characteristic testing methods for alkali-activated materials: A review. J Building Eng. 2023;75:106830.
19. Dener M, Karatas M, Shi JY, Mohabbi M. Mechanical properties and microstructure of hybrid alkali-activated cement component. Arch Civ Mech Eng. 2024;25(1).
20. Kiliç D, Öz A, Benli A, Tortum A, Kaplan G, Aydin AC. Integration of reclaimed asphalt aggregates into glass fiber-reinforced alkali-activated composites: Mechanical performance and durability. Constr Build Mater. 2025;458.
21. Zhang B, Zhu H, Feng P, Zhang P. A review on shrinkage-reducing methods and mechanisms of alkali-activated/geopolymer systems: effects of chemical additives. J Building Eng. 2022;49.
22. Toklu K, Aydin B, Demir I, Demir S, Günel G, Sevim Ö. Ambient-cured alkali-activated geopolymer mortars: influence of activator molarity and fly ash replacement on microstructure and mechanical performance. Arch Civ Mech Eng. 2026;26(2):36.
23. Sun BB, Ye G, de Schutter G. A review: Reaction mechanism and strength of slag and fly ash-based alkali-activated materials. Constr Build Mater. 2022;326:126843.
24. Behfarnia K, Rostami M. An assessment on parameters affecting the carbonation of alkali-activated slag concrete. J Clean Prod. 2017;157:1–9.
25. Wang WS, Zhang P, Dai XB, Zheng YX, Hu SW. Workability of self-compacting geopolymer concrete: The effect of nano-SiO2 and steel-polyvinyl alcohol hybrid fiber. Constr Build Mater. 2025;460:139849.
26. Li B, Li KH, Zhou YW, Xu H, Zhao CH, Yu Y, Li ZC. Nano-mechanism of graphene oxide reinforced fly ash-slag based geopolymer materials to form high polymerization degree C-(A)-S-H: A new view of physical-chemical synergistic effect. Cem Concrete Comp. 2025;157:105.
27. Ahmed HU, Mohammed AA, Mohammed AS. Effectiveness of nano-SiO2 on the mechanical, durability, and microstructural behavior of geopolymer concrete at different curing ages. Arch Civ Mech Eng. 2023;23(2):129.
28. Amiri Y, Hassaninasab S, Chehri K, Zahedi M. Investigating the effect of adding bacillus bacteria and nano-clay on cement mortar properties. Case Stud Constr Mater. 2022;17:e01167.

29. Raj RS, Arulraj GP, Anand N, Kanagaraj B, Lubloy E, Naser MZ. Nanomaterials in geopolymer composites: a review. Dev Built Environ. 2023;13:00114.
30. Niu XJ, Li QB, Hu Y, Tan YS, Liu CF. Properties of cement-based materials incorporating nano-clay and calcined nano-clay: a review. Constr Build Mater. 2021;284:122820.
31. Hakamy A, Shaikh F, Low IM. Characteristics of nanoclay and calcined nanoclay-cement nanocomposites. Compos Part B Eng. 2015;78:174–84.
32. Nazir MS, Mohamad Kassim MH, Mohapatra L, Gilani MA, Raza MR, Majeed K. Characteristic properties of nanoclays and characterization of nanoparticulates and nanocomposites, Nanoclay reinforced polymer composites: Nanocomposites and bionanocomposites, Springer; 2016, pp. 35–55.
33. Assaedi H, Shaikh FUA, Low IM. Effect of nano-clay on mechanical and thermal properties of geopolymer. J Asian Ceram Soc. 2016;4(1):19–28.
34. Shahrajabian F, Behfarnia K. The effects of nano particles on freeze and thaw resistance of alkali-activated slag concrete. Constr Build Mater. 2018;176:172–8.
35. Gadkar A, Subramaniam KVL. Rheology control of alkali-activated fly ash with nano clay for cellular geopolymer application. Constr Build Mater. 2021;283:122687.
36. Mabrouk A, Raza A, Elhadi KM, Ahmed B, Kubica J, Chen WS. Effect of curing temperature, silica fume, and waste tire rubber aggregate on material characterization of lightweight geopolymer composite. Constr Build Mater. 2024;453.
37. Mujdeci A, Guo Y, Bompa D, Elghazouli A. Performance of circular steel tubes infilled with rubberised concrete under cyclic loads. Eng Struct. 2024;302:117327.
38. Thomas BS, Gupta RC. A comprehensive review on the applications of waste tire rubber in cement concrete. Renew Sust Energ Rev. 2016;54:1323–33.
39. Siddique R, Naik TR. Properties of concrete containing scrap-tire rubber - an overview. Waste Manage. 2004;24(6):563–9.
40. Mohammadi I, Khabbaz H, Vessalas K. Enhancing mechanical performance of rubberised concrete pavements with sodium hydroxide treatment. Mater Struct. 2016;49(3):813–27.
41. Gupta T, Chaudhary S, Sharma RK. Assessment of mechanical and durability properties of concrete containing waste rubber tire as fine aggregate. Constr Build Mater. 2014;73:562–74.
42. Mohajerani A, Burnett L, Smith JV, Markovski S, Rodwell G, Rahman MT, Kurmus H, Mirzababaei M, Arulrajah A, Horpibulsuk S, Maghool F. Recycling waste rubber tyres in construction materials and associated environmental considerations: a review. Resour Conserv Recy. 2020;155.
43. Bascetin A, Adiguzel D, Eker H, Tuylu S. The investigation of geochemical and geomechanical properties in surface paste disposal by pilot–scale tests. Int J Min Reclam Environ. 2022;36(8):537–51.
44. Khern YC, Paul SC, Kong SY, Babafemi AJ, Anggraini V, Miah MJ, Savija B. Impact of chemically treated waste rubber tire aggregates on mechanical, durability and thermal properties of concrete. Front Mater. 2020;7.
45. Paul SC, Islam S, Al Mamun A, Islam N, Babafemi AJ, Kong SY, Miah MJ. Treated waste tire using cement coating as coarse aggregate in the production of sustainable green concrete. Eng Basel. 2023;4(2):1432–45.
46. Dehdezi PK, Erdem S, Blankson MA. Physico-mechanical, microstructural and dynamic properties of newly developed artificial fly ash based lightweight aggregate - Rubber concrete composite. Compos Part B-Eng. 2015;79:451–5.
47. Singaravel DA, Veerapandian P, Rajendran S, Dhairiyasamy R. Enhancing high-performance concrete sustainability: integration of waste tire rubber for innovation. Sci Rep-UK. 2024;14(1).
48. Bayraktar OY, Yakupoglu U, Benli A. Slag/diatomite-based alkali-activated lightweight composites containing waste andesite sand: mechanical, insulating, microstructural and durability properties. Arch Civ Mech Eng. 2023;23(4).
49. Murali G, Wong LS, Karthikeyan K, Abdellatief M, Dixit S. Concrete resilience under the impact of water forces: a review of abrasion resistance in hydraulic structures. Results Eng. 2025;26:104654.
50. Murali G, Wong LS, Abdulkadir I, Algaifi HA, Abdellatief M. Sustainable transformation of waste phosphogypsum into geopolymer concrete: Comprehensive review on strength, durability, and microstructural characteristics. J Building Eng. 2025;111.
51. Ameri F, Shoaei P, Zareei SA, Behforouz B. Geopolymers vs. alkali-activated materials (AAMs): A comparative study on durability, microstructure, and resistance to elevated temperatures of lightweight mortars. Constr Build Mater. 2019;222:49–63.
52. Huang JJ, Li J, Shao RZ, Wu CQ. Effect of high temperature and cooling method on compression and fracture properties of geopolymer-based ultra-high performance concrete. J Building Eng. 2025;105:112433.
53. Li J, Wu S, Shi Y, Huang Y, Tian Y, Yagaanbuyant D. Effects of nano-SiO2 on sulfate attack resistance of multi-solid waste-based alkali-activated mortar. Case Stud Constr Mater. 2025;22:e04227.
54. Mohseni E, Kazemi MJ, Koushkbaghi M, Zehtab B, Behforouz B. Evaluation of mechanical and durability properties of fiber-reinforced lightweight geopolymer composites based on rice husk ash and nano-alumina. Constr Build Mater. 2019;209:532–40.
55. Efe M, Öz A, Bayrak B, Kaplan G, Aydın AC. Effect of Na2SiO3/NaOH rate and natural zeolite content on basalt fiber reinforced eco-efficient slag-based geopolymer mortar synthesis. Arch Civ Mech Eng. 2024;24(4):215.

56. Abdelmonim A, Bompa DV. Mechanical and fresh properties of multi-binder geopolymer mortars incorporating recycled rubber particles. Infrastructures-Base. 2021;6(10).
57. ASTM. ASTM C348–19 Standard test method for flexural strength of hydraulic-cement mortars. West Conshohocken, PA.: ASTM International; 2019.
58. ASTM. ASTM C349–18 Standard test method for compressive strength of hydraulic-cement mortars (using portions of prisms broken in flexure). ASTM International, West Conshohocken, PA, 2018.
59. ASTM C642–13 Standard Test Method for Density, Absorption, and Voids in Hardened Concrete. West Conshohocken, PA: ASTM International. 2013.
60. Alcan HG, Benli A, Öz A, Bayrak B, Kaplan G, Aydin AC. Effective utilization of silica fume and waste colemanite in eco-sustainable prepacked geopolymers. Constr Build Mater. 2024;457.
61. Bayraktar OY, Özel HB, Benli A, Yilmazoglu MU, Türkel IH, Dal BB, Sevik H, Kaplan G. Sustainable foam concrete development: Enhancing durability and performance through pine cone powder and fly ash incorporation in alkali-activated geopolymers. Constr Build Mater. 2024;457.
62. EN 1015-18. Methods of test for mortar for masonry – part 18: determination of water absorption coefficient due to capillary action of hardened mortar. Brussels, Belgium: European Committee for Standardization (CEN); 2002.
63. ASTM C666/C666M-15. Standard test method for resistance of concrete to rapid freezing and thawing. ASTM International, West Conshohocken, PA, 2015.
64. Dejaeghere I, Sonebi M, De Schutter G. Influence of nano-clay on rheology, fresh properties, heat of hydration and strength of cement-based mortars. Constr Build Mater. 2019;222:73–85.
65. Farzadnia N, Ali AAA, Demirboga R, Anwar MP. Effect of halloysite nanoclay on mechanical properties, thermal behavior and microstructure of cement mortars. Cem Concr Res. 2013;48:97–104.
66. Shilar FA, Ganachari SV, Patil VB, Khan TMY, Almakayeel NM, Alghamdi S. Review on the relationship between nano modifications of geopolymer concrete and their structural characteristics. Polymers-Basel. 2022;14(7):1421.
67. Zidi Z, Ltifi M, Zafar I. Comparative study: nanosilica, nanoalumina, and nanozinc oxide addition on the properties of localized geopolymer. J Aust Ceram Soc. 2021;57(3):783–92.
68. Hakamy A, Shaikh F, Low I. Thermal and mechanical properties of NaOH treated hemp fabric and calcined nanoclay-reinforced cement nanocomposites. Mater Design. 2015;80:70–81.
69. Heikal M, Ibrahim NS. Hydration, microstructure and phase composition of composite cements containing nanoclay. Constr Build Mater. 2016;112:19–27.
70. Youssf O, Elchalakani M, Hassanli R, Roychand R, Zhuge Y, Gravina RJ, Mills JE. Mechanical performance and durability of geopolymer lightweight rubber concrete. J Building Eng. 2022;45 .
71. Bao JW, Wang YW, Zhang P, Zhang XY, Cui YF. The role of internally incorporated nano-silica in recycled aggregate concrete: modification of transport properties. Constr Build Mater. 2023;371.
72. John SK, Nadir Y, Cascardi A, Arif MM, Girija K. Effect of addition of nanoclay and SBR latex on fly ash-slag geopolymer mortar. J Building Eng. 2023;66:105875.
73. Deb PS, Sarker PK, Barbhuiya S. Effects of nano-silica on the strength development of geopolymer cured at room temperature. Constr Build Mater. 2015;101:675–83.
74. Yang L, Zhu Z, Sun H, Zhang X, Liu J, Pan J, Ma B, Huo W. Modification mechanism of nano-SiO2 and LSS-1 ions on geopolymer-solidified soil: mechanism of microstructure and frost resistance. Arch Civ Mech Eng. 2025;25(5):256.
75. Adak D, Sarkar M, Mandal S. Effect of nano-silica on strength and durability of fly ash based geopolymer mortar. Constr Build Mater. 2014;70:453–9.
76. Li LG, Zheng JY, Ng PL, Kwan AKH. Synergistic cementing efficiencies of nano-silica and micro-silica in carbonation resistance and sorptivity of concrete. J Building Eng. 2021;33:101862.
77. Seifan M, Mendoza S, Berenjian A. Mechanical properties and durability performance of fly ash based mortar containing nano- and micro-silica additives. Constr Build Mater. 2020;252:119121.
78. Ghone MO, Long GC, Yang K, Ma XN, Islam N. Toughness improvement of low strength ceramsite lightweight concrete by polypropylene fiber and recycled rubber particle. Constr Build Mater. 2024;422.
79. Aragoncillo AM, Cleary D, Thayasivam U, Lomboy G. Water sorptivity prediction model for concrete with all coarse recycled concrete aggregates. Constr Build Mater. 2023;394:132128.
80. Paktiawal A, Alam M. Experimental evaluation of sorptivity for high strength concrete reinforced with zirconia rich glass fiber and basalt fiber. Mater Today Proc. 2022;49:1132–40.
81. Benli A, Karatas M, Bakir Y. An experimental study of different curing regimes on the mechanical properties and sorptivity of self-compacting mortars with fly ash and silica fume. Constr Build Mater. 2017;144:552–62.
82. Bayraktar OY, Yarar G, Benli A, Kaplan G, Gencel O, Sutcu M, Kozlowski M, Kadela M. Basalt fiber reinforced foam concrete with marble waste and calcium aluminate cement. Struct Concrete. 2023;24(1):1152–78.
83. Kaplan G, Coskan U, Benli A, Bayraktar OY, Kucukbaltaci AB. The impact of natural and calcined zeolites on the mechanical and durability characteristics of glass fiber reinforced cement composites. Constr Build Mater. 2021;311:125336.

84. Turkoglu M, Bayraktar OY, Benli A, Kaplan G. Effect of cement clinker type, curing regime and activator dosage on the performance of one-part alkali-activated hybrid slag/clinker composites. J Building Eng. 2023;68:106164.
85. Arab MAE-S, Mohamed AS, Taha MK, Nasr A. Microstructure, durability and mechanical properties of high strength geopolymer concrete containing calcinated nano-silica fume/nano-alumina blend. Constr Build Mater. 2025;472:140903.
86. Dener M, Altunhan U, Benli A. A green binder for cold weather applications: enhancing mechanical performance of alkali-activated slag through modulus, alkali dosage, and Portland cement substitution. Arch Civ Mech Eng. 2024;24(3).
87. Cheng GW, Zhang ZJ, Mao RY, Wu HW, Liang X, Zhou JR. Experimental investigation on thermal and mechanical performance of alkali-activated coal gangue foam materials doped with phosphogypsum. Arch Civ Mech Eng. 2025;25(3).
88. Hassaan MM, Khater HM, El-Mahllawy MS. El Nagar, Production of geopolymer composites enhanced by nano-kaolin material. J Adv Ceram. 2015;4(4):245–52.
89. Khater HMM, Gawwad HAA. Synthesis and characterization of MK/Slag geopolymer composites enhanced by various ratios of nano kaolin. Epitoanyag. 2017;69(2):40–8.
90. Song QF, Guo MZ, Ling TC. A review of elevated-temperature properties of alternative binders: Supplementary cementitious materials and alkali-activated materials. Constr Build Mater. 2022;341.
91. Liu H, Jing W, Qin LL, Duan P, Zhang ZH, Guo R, Li WL. Thermal stability of geopolymer modified by different silicon source materials prepared from solid wastes. Constr Build Mater. 2022;315.
92. Ma QK, Mao ZH, Zhang JC, Du GF, Li YQ. Behavior evaluation of concrete made with waste rubber and waste glass after elevated temperatures. J Building Eng. 2023;78.
93. Bayraktar OY, Bozkurt TH, Benli A, Koksal F, Tuerkoglu M, Kaplan G. Sustainable one-part alkali activated slag/fly ash Geo-SIFCOM containing recycled sands: Mechanical, flexural, durability and microstructural properties. Sustain Chem Pharm. 2023;36.
94. Aly M, Hashmi MSJ, Olabi AG, Messeiry M, Hussain AI. Effect of nano clay particles on mechanical, thermal and physical behaviours of waste-glass cement mortars. Mat Sci Eng A Struct. 2011;528(27):7991–8.
95. Bodur B, Benli A, Bayraktar OY, Alcan HG, Kaplan G, Aydin AC. Impact of attapulgite and basalt fiber additions on the performance of pumice-based foam concrete: mechanical, thermal, and durability properties. Arch Civ Mech Eng. 2025;25(2).
96. Çevik A, Alzeebaree R, Humur G, Nis A, Gülsan ME. Effect of nano-silica on the chemical durability and mechanical performance of fly ash based geopolymer concretevol. Ceramics Int. 2018;45(11):14479–14479.
97. Mansi A, Sor NH, Hilal N, Qaidi SM. The impact of nano clay on normal and high-performance concrete characteristics: a review. IOP Conf Ser Earth Environ Sci. 2022;012085.
98. Deng Z. Influence of recycled rubber and glass aggregates on magnesium sulfate resistance of geopolymers: physio-mechanical properties and mechanisms. Constr Build Mater. 2024;438:137134.
99. Moghaddam SC, Madandoust R, Jamshidi M, Nikbin IM. Mechanical properties of fly ash-based geopolymer concrete with crumb rubber and steel fiber under ambient and sulfuric acid conditions. Constr Build Mater. 2021;281.
100. Khawaji M. Hydration, microstructure, and properties of fly ash-based geopolymer: a review. Mater Sci-Poland. 2023;41(2):263–87.
101. Xiao R, Shen ZL, Si RZ, Polaczyk P, Li YC, Zhou HY, Huang BS. Alkali-activated slag (AAS) and OPC-based composites containing crumb rubber aggregate: Physico-mechanical properties, durability and oxidation of rubber upon NaOH treatment. J Clean Prod. 2022;367.
102. Su E, Dong W, Yin Y. Study on compressive strength and pore structure evolution of nano-silica modified aeolian sand concrete under freeze–thaw cycle based on fractal dimension. Struct Concrete. 2025.
103. Fan YF, Zhang SY, Wang Q, Shah SP. Effects of nano-kaolinite clay on the freeze-thaw resistance of concrete. Cem Concrete Comp. 2015;62:1–12.
104. Öz A, Kiziloglu E, Benli A, Kaplan G. Enhancing freeze-thaw and sulfate resistance of expanded perlite-based alkali-activated lightweight composites with waste tire aggregates and brick powder. Arch Civ Mech Eng. 2025;26(1).
105. Qin C, Xun K, Yuan Q, Zhang M, Hua Q, Wu T, Zhou B. Study on the flexural performance of 4D steel fiber-reinforced concrete under freeze-thaw cycles. Constr Build Mater. 2026;514:145619.
106. Bayraktar OY, Soylemez H, Kaplan G, Benli A, Gencel O, Turkoglu M. Effect of cement dosage and waste tire rubber on the mechanical, transport and abrasion characteristics of foam concretes subjected to H2SO4 and freeze–thaw. Constr Build Mater. 2021;302:124229.
107. Bayraktar OY, Benli A, Bodur B, Öz A, Kaplan G. Performance assessment and cost analysis of slag/metakaolin based rubberized semi-lightweight geopolymers with perlite aggregate: Sustainable reuse of waste tires. Constr Build Mater. 2024;411.
108. Türkel I, Yilmazoglu MU, Alman MA, Benli A, Bayraktar OY, Kaplan G. Synergistic effects of boiler ash and polypropylene fibers on the mechanical and durability properties of fly ash-based geopolymer foam concrete. Arch Civ Mech Eng. 2025;26(1).
109. Khazaleh MA, Karumanchi M, Bellum RR. Stabilization of soils with nanoclay subjected to freeze-thaw cycles. Nanatechnol Environ Eng. 2023;8(1):237–51.

110. Chen C, Zhang RY, Zhou L, Wang YB. Influence of waste tire particles on freeze-thaw resistance and impermeability performance of waste tires/sand-based autoclaved aerated concrete composites. Buildings. 2022;12(1).
111. Bulut H, Kandil U. Investigation of freeze-thaw performance for sustainable rubberized concrete composites with different water to cement ratios. Materiales de Construcción. 2025;75(357).
112. Saviour MN, Technology. Environmental impact of soil and sand mining: a review. Int J Sci Environ. 2012;1(3):125–34.
113. Edun A, Hachem-Vermette C. Energy and environmental impact of recycled end of life tires applied in building envelopes. J Building Eng. 2021;39:102242.
114. Gamal HA, El-Feky MS, Alharbi YR, Abadel AA, Kohail M. Enhancement of the Concrete Durability with Hybrid Nano Materials. Sustainability-Basel 13(3) (2021).
115. Li JY, Si JW, Luo F, Zuo CX, Zhang PP, Sun YB, Li WQ, Miao SD. Self-compensating geopolymer utilizing nano-clay and chopped basalt fibers. Constr Build Mater. 2022;357.
116. Zhang YW, Zhou CL, Song JX, Li JY, Gong YF. Foundry waste reutilization: Anti-shrinkage geopolymer based on nano-clay and coal gangue. Constr Build Mater. 2024;434.
117. Provis JL. Alkali-activated materials. Cem Concr Res. 2018;114:40–8.
118. Yang K-H, Song J-K, Song K-I. Assessment of CO2 reduction of alkali-activated concrete. J Clean Prod. 2013;39:265–72.
119. Lee BX, Kjaerulf F, Turner S, Cohen L, Donnelly PD, Muggah R, Davis R, Realini A, Kieselbach B, MacGregor LS. Transforming our world: implementing the 2030 agenda through sustainable development goal indicators. J Public Health Policy. 2016;37(1):13–31.
120. Jessop PG, Trakhtenberg S, Warner J. The twelve principles of green chemistry, ACS Publications, 2009.

Publisher's note Springer Nature remains neutral with regard to jurisdictional claims in published maps and institutional affiliations.

Springer Nature or its licensor (e.g. a society or other partner) holds exclusive rights to this article under a publishing agreement with the author(s) or other rightsholder(s); author self-archiving of the accepted manuscript version of this article is solely governed by the terms of such publishing agreement and applicable law.

Authors and Affiliations

Ahmet Benli[1] · Bayram Sönmez[1] · Ali Öz[2,3] · Adem Yar[4] · Oğuzhan Yavuz Bayraktar[5] · Gökhan Kaplan[2]

✉ Ahmet Benli
ahbenli@hotmail.com

[1] Department of Civil Engineering, Bingol University, Bingol 12100, Turkey

[2] Department of Civil Engineering, Atatürk University, Erzurum 25030, Turkey

[3] Narman Vocational School, Atatürk University, Erzurum 25530, Turkey

[4] Department of Mechanical Engineering, Bingol University, Bingol 12100, Turkey

[5] Department of Civil Engineering, Kastamonu University, Kastamonu 37150, Turkey